# Quantitative assessment of moisture source and temperature governing rainfall $\delta^{18}O$ from 20 years long monitoring records in SW-France: Importance for isotopic-based climate reconstructions

Jian Zhang [a, b]*, Dominique Genty [a]*, Colette Sirieix [b], Simon Michel [a], Bénédicte Minster [c], Edouard Régnier [c]

[a] *Environnements et Paléoenvironnements Océaniques et Continentaux (EPOC), UMR CNRS, 5805, Université de Bordeaux, 33615 Pessac Cedex, France*

*b CNRS, Arts et Metiers Institute of Technology, Bordeaux INP, INRAE, I2M Bordeaux, Université de Bordeaux, 33400 Talence, France*

[c] *Laboratoire de Sciences du Climat et de l'Environnement (LSCE), Orme des Merisiers, UMR 8212 CEA/CNRS/UVSQ, 91191 Gif-sur-Yvette Cedex, France*

**Submitted the minor revised version to Journal of hydrology**

First author: Jian Zhang

* The corresponding author: Jian Zhang and Dominique Genty

E-mail: jian.zhang@u-bordeaux.fr and dominique.genty@u-bordeaux.fr

Postal Address: Allée Geoffroy Saint-Hilaire Bât. NB18, Université de Bordeaux, Pessac, France

## Abstract

In the mid-high latitude region, variations of stable isotopic compositions of atmospheric precipitation ($\delta^{18}O_p$ and $\delta D_p$) were commonly regarded as reflecting a "temperature effect". However, some studies have indicated that the change of moisture source was an important controlling factor for $\delta^{18}O_p$. To clarify whether there is connection between $\delta^{18}O_p$ and the variation of moisture source in Southwest France (SW-France), whose implication for speleothem paleoclimatic interpretation is of great importance, we have used among the longest isotopic time series from SW-France (Le Mas and Villars stations) and a 5 days' reconstruction of air mass history during the 1997-2016 A.D period based on HYSPLIT tracking model. We found the percentage of initial moisture sources (PIMS) as an important factor controlling the oxygen isotope composition of precipitation in SW-France, whether monthly or inter-annual timescales was considered. Additionally, we found that the $\delta^{18}O_p$ preserved the signal of local temperature, supporting a "temperature effect", while no evidence for its "amount effect" have been observed. These quantified links between PIMS/local-temperature and $\delta^{18}O_p$ appears useful to better understand the links between stable oxygen isotopes and climate parameters. Our long-term monitoring of the $\delta^{18}O_p$, d-excess, and moisture sources reveals decadal trends, highlighting a tight coupling in hydrologic systems and relatively fast changes in SW-France rainfall sources controlled by atmospheric circulations.

**Keywords:** Rainfall; Isotope ratios; HYSPLIT model; Moisture Sources; Temperature; Southwest France

# Main manuscript content

## 1. Introduction

The stable isotopic compositions of atmospheric precipitation ($\delta^{18}O_p$ and $\delta D_p$) (See acronyms in Appendix Table 1) are important tools for understanding regional atmospheric circulation and local hydrological cycle (Dansgaard, 1964; Sharp, 2007; Gat, 2010; Genty et al., 2014). The mechanism between the temperature/precipitation and isotope ratios in rainfall are considerably complex, including these processes like Rayleigh fractionation, diffusive exchange of isotopes between raindrops and vapor, as well as re-evaporation of falling rainfall (Fricke and O'Neil, 1999; Araguás-Araguás et al., 2000, 2005; Risi et al., 2008; Lachniet, 2009; Field et al., 2010). The $\delta^{18}O$ in many natural archives has been used to reconstruct the paleoenvironment over the past few years (Pettit et al., 1999; Wang et al., 2001; Hu et al., 2008; Zhang et al., 2008; MeDermott et al., 2011). Thus, the investigation and qualification on the various factors governing the rainfall stable isotopes are of great importance for the paleoclimate community (Krklec and Domínguez-Villar., 2014; Krklec et al., 2018).

Average monthly local temperatures, generally measured 2 m above ground level, are statistically correlated with the monthly $\delta^{18}O_p$ and $\delta D_p$ on middle and high-latitude monitoring stations, called "temperature effect" (Dansgaard, 1964; IAEA working group, 2000), particularly obvious on the European continent (Krklec and Domínguez-Villar., 2014; Krklec et al., 2018), however, the relationship on the inter-annual timescale remains unclear. Additionally, some researchers have revealed that the inter-annual atmospheric variability, such as North Atlantic Oscillation (NAO), also controls the rainfall isotopic value (Baldini et al., 2008; Fischer and Mattey, 2012). However, local precipitation amount and monthly isotope ratios do not exhibit significant correlations in continental Europe (Dansgaard, 1964).

Some previous studies have proposed that the moisture source was an important controlling factor for $\delta^{18}O_p$ and $\delta D_p$ (Cruz et al., 1992; Cole et al., 1999; Friedman et al., 2002; Lachniet, 2009). Moisture source location is generally estimated by the calculation of the deuterium excess (d-excess), which is significatively different between the Atlantic Ocean and the Mediterranean Sea (Dansgaard, 1964; Craig and Gordon, 1965; Vimeux et al., 1999; Uemura et al., 2012). Moreover, d-excess also reflect the variation on near-surface relative humidity (RH) during evaporation and moisture source temperature variations (Pfahal and Sodemann, 2014). However, by using this method, it is extremely difficult to quantify the pathway of water vapor transportation, limiting the understanding of the change of moisture source for $\delta^{18}O_p$ and $\delta D_p$, particularly for spatial and temporal evapotranspiration (ET) contributions.

To overcome this issue, the history of air masses have been calculated by studying regional/general circulation using Lagrangian models. However, obvious discrepancies between observed isotopes and the variation of modeled air masses were questioned, which may be due to insufficient accuracy of the models (Hoffmann et al., 1998; Sturm, 2005; Schmidt et al., 2007; Sodemann et al., 2008; Pfahl and Wernli, 2008; Langebroek et al., 2011). Therefore, this raised question of how to accurately quantify the variability of initial moisture sources, which are important for explaining the climatic significance of $\delta^{18}O_p$ and $\delta D_p$ (Aggarwal et al., 2004; Dayem et al., 2010; Domínguez-Villar et al., 2017).

The Hybrid Single-Particle Lagrangian Integrated Trajectory (HYSPLIT) model (Draxler and Hess, 1998), an advanced system calculating air parcel trajectories, has been greatly promoted (Stein et al., 2015). This atmospheric calculation model based on the Eulerian and hybrid Lagrangian approaches can accurately reflect the variation of moisture source (Stein et al., 2015). Among them, the Lagrangian method is using a moving framework as references for the calculations of diffusion and advection when the trajectories or air parcels move from initial source region, and the Eulerian methodology is using a restricted three-dimensional grid cell to compute air concentrations (Stein et al., 2015). Additionally, HYSPLIT software has been successfully applied in several studies including tracking the atmospheric circulation change (Sjostrom and Welker, 2009; Breitenbach et al., 2010; Abouelmagd et al., 2012; Dumitru et al., 2017; Sánchez‐Murillo et al., 2020),

predicting the direction of pollutant diffusion (Chen et al., 2012) and monitoring wildfire smoke (Rolph et al. 2009).

In Southwest France (SW-France), there are very few published data concerning stable isotopes of precipitation, especially for long time-series (i.e. > 10 years). Our research sites, including Le Mas and Villars stations, are situated on karst areas, and rainfall isotope ratios (e.g. $\delta^{18}O_p/\delta D_p$) are regarded as a good tool to determine the sources of the seepage water (Ladouche et al., 2009) and its variations in time and consequences on isotopic cave calcite composition (speleothems) (Genty et al., 2001, 2006, 2014; Genty, 2008). More importantly, this area is a key place for studying the moisture pathways from the North Atlantic and the Mediterranean across the European continent (Duffourg and Ducrocq, 2011), and our long-term observations for the rainfall $\delta^{18}O_p$ as well as its environment parameters allow us to confidential understand the local hydrological cycle and climate change.

In summary, there are the following unresolved scientific limitations about the stable isotopic composition of the rainfall in SW-France, including: **(1)** unclear relationships and mechanisms between initial moisture sources and $\delta^{18}O_p$ on the monthly and inter-annual timescales. **(2)** unquantified links between $\delta^{18}O_p$ and various controlling factors (temperature, rainfall and moisture source). Here, we combined with $\delta^{18}O_p$ in SW-France, the data of moisture sources and regional/local climatic parameters, addressing these above-mentioned scientific questions. Our study attempts to determine the variation of initial moisture sources and its relation to the

stable isotopic composition of the rainfall in the SW-France using the HYSPLIT model. The link between $\delta^{18}O_p$ and various controlling factors was also quantified to eventually calibrate the link between local climate parameters and $\delta^{18}O_p$ as well as deepen understanding for the significance of cave speleothem $\delta^{18}O$.

## 2. Study area

Rainfall samples were collected from two monitoring sites, namely Le Mas (45°7′45″N, 1°11′31″E) and Villars (45°26′18″N, 0°47′2″E) (Figs. 1A and B) about 20 km far each other. During the monitoring period from 1997-2016, the mean annual amount of precipitation at the Villars station is 1003 mm (Standard Deviation:150 mm), and the mean annual temperature is 12.5 °C. The region is composed of limestone characterized by numerous carbonate caves, among them, Villars Cave was extensively studied for its speleothems and cave environment (Genty et al., 2003, 2006, 2010, 2014; Genty, 2008).

The large-scale atmospheric circulation in Western Europe (WE) is affected by climatic system influences from different geographic area, such as Atlantic, Mediterranean, Greenland and European Continents (Giuntoli et al., 2013). The most important circulation pattern is considered to be the winter North Atlantic Oscillation (NAO) which is a driver for streamflow in North and West Europe (Trigo et al., 2002). Other large-scale circulation patterns, such as the Arctic Oscillation (AO) or Atlantic

143 Multidecadal Oscillation (AMO) have also influenced the climatic variation in West
144 Europe region (O'Reilly et al., 2016).

145 In order to better quantify the spatial distribution of initial moisture source, the
146 research region was divided into six sections (Fig. 1A; Appendix Table 1), namely
147 Proximal Atlantic and West Europe (PAWE), Distal Atlantic (DA), North Atlantic
148 (NA), North America and Greenland (NAGR), Mediterranean (ME), Northern
149 European and Northern Atlantic (NENA) (referred and modified from Krklec and
150 Domínguez-Villar, 2014). These different regions have been defined on the basis of
151 European geographical limitations (e.g. ocean-continent borders and ocean boundary)
152 and distribution patterns of the initial seawater isotopic composition as well as the
153 concentrated locations of moisture sources (Fig. 1A; Lachniet, 2009; Krklec and
154 Domínguez-Villar, 2014).

155 ## 3. Methods and data

156 ### 3.1 Stable isotopic composition of rainwater

157 The stable isotopic samples were collected in the Le Mas and Villars stations at
158 an approximately monthly scale during the period from 1997 to 2016. Rainfall
159 sampling protocol follows the recommended principles from Global Network of
160 Isotope in Precipitation (GNIP) from the International Atomic Energy Agency
161 (IAEA). The rainwater is collected in a 5 L tank with a funnel. Before the tank is
162 buried in the soil, each sample have added a few ml of liquid paraffin to prevent any

163 evaporation. Water is collected into a 15 ml glass bottle which is closed by a specific
164 cork with a conical funnel making sure waterproofness.

165 The hydrogen isotopic composition (δD) of the precipitation sample was
166 measured on an ISO-PRIME mass spectrometer and a PICARRO laser spectrometer,
167 and the analytical absolute error for δD is ±0.5 ‰. The oxygen isotopes ($\delta^{18}O$) were
168 measured on a Finnigan MAT 252 by equilibration with $CO_2$, with an analytical error
169 of ±0.05‰. In order to avoid potential paraffin pollution, all measured samples were
170 filtered through 0.2μm Anlypore filters. On the PICARRO spectrometer, the memory
171 effect was treated by doing 6 to 7 times' successive measurements of the same
172 sample, and by keeping only the last 3 results to determine the value of rainfall δD.
173 For the calibration, we used an internal EPB standard (Laboratoire de Sciences du
174 Climat et de l'Environnement: LSCE) as working reference standards that was
175 cross-checked. The final result of $\delta^{18}O$ and δD are then expressed relative to the
176 Vienna Standard Mean Ocean Water (V-SMOW). Early measurements in 1997 and
177 1998 were measured on a VG SIRA IRMS with an error of ±0.2‰ for the $\delta^{18}O$ while
178 δD was performed using the zinc reduction method with an error close to ±2‰ (Genty
179 et al., 2014).

180 **3.2 Meteorological data**

181 European precipitation data was downloaded from the Global Precipitation
182 Climatology Project (GPCP) Version 2.3 combining observations and satellite pr

ecipitation data with 2.5°x2.5° global grids (Website: https://www.esrl.noaa.gov/psd /data/gridded/data.gpcp.html). The air temperature data were obtained from the J ones CRU Air Temperature Anomalies Version 4 with 5°x5° global grids (Webs ite: https://www.esrl.noaa.gov/psd/data/gridded/data.crutem4.html). The sea surface temperature (SST) data were obtained from Kaplan Extended SST Version 2 with 5°x5° global grids (https://psl.noaa.gov/data/gridded/data.kaplan_sst.html). Th e NAO index was downloaded from the following official websites: https://ww w.ncdc.noaa.gov/teleconnections/nao/data.csv.

## 3.3 HYSPLIT model for tracking moisture source

To diagnose the moisture transportation pathways and better understand the $\delta^{18}O_p$ variability in SW-France, we employed the method of back trajectories of air parcels from the NCEP reanalysis data (Website: ftp://arlftp.arlhq.noaa.gov/pub/archives/reanalysis). The HYSPLIT model was downloaded from the NOAA Air Resources Laboratory (Website: http://ready.arl.noaa.gov/HYSPLIT.php) (Draxler and Rolph, 2010). In order to analyze the temporal variability of moisture sources, we have divided a year into four seasons: spring (March–May), summer (June–August), autumn (September–November), and winter (December–February of the following year).

Previous studies have revealed that trajectories with the average residence time of water vapor in the atmosphere are 120 hours (5 days) (Numaguti, 1999; Krklec and Domínguez-Villar, 2014). Therefore, the variation of moisture sources were identified

in the Villars station (we assumed a common source for Le Mas station being very close to Villars) during the previous 120 h (5 days) (Krklec and Domínguez-Villar, 2014; Krklec et al., 2018). The water vapor transportation usually occurs mainly at 1500m-3000m (above ground level: a.g.l) in the mid-low troposphere, however, the peak value of water vapor transportation in the plain is an at altitude of about 1500 m (~ 850 hPa) (Tang et al., 2015; Cai et al., 2017). Moreover, the back trajectories from different elevations showed similar paths and regulations (Krklec and Domínguez-Villar, 2014; Krklec et al., 2018), therefore we consider the only altitude of 1500 m (a.g.l) as the initial vertical height for the water vapor transportation.

The integrated system was operated for computing the daily trajectory at the time of 00:00, 06:00, 12:00 and 18:00, and the output of trajectories are made every 6 hours. The cluster analysis tool was applied for integrating all trajectories, which were grouped according to the horizontal moving speed and direction in HYSPLIT model (Tang et al., 2015). Finally, HYSPLIT4 software is used for superposition analysis and designed to get the diagram to determine the variation of the initial moisture source.

## 3.4 Statistical methods and packages

The correlations between regional parameters and $\delta^{18}O_p$ variability in SW-France were calculated using R programming. Significance levels for correlations were calculated using Student t-tests. Degrees of freedom corrections were calculated by time-series autocorrelations (McCarthy et al., 2015):

$$Neff=N*((1-ax*ay)/(1+ax*ay))$$

where Neff is the corrected degrees of freedom of Student t statistics, N is the length of the time series, and ax, ay are the first order autocorrelation of each time-series.

The links between PIMS/temperature and $\delta^{18}O_p$ were established using multiple linear regression analysis methods by Statistical Package for the Social Sciences (SPSS) software:

$$y_i=\beta_0+\beta_1 x_{i1}+\beta_2 x_{i2}+...+\beta_p x_{ip}+\epsilon$$

where, for $i$ denotes $n$ factors; $y_i$ denotes dependent variable; $x_i$ denotes explanatory variables; $\beta_0$ denotes y-intercept; $\beta_p$ denotes slope coefficients for each explanatory variable; $\epsilon$ denotes residuals.

# 4. Results

## 4.1 Relationship between $\delta^{18}O_p$ and local/regional climate parameters

The correlation of the $\delta^{18}O_p$ between Villars and Le Mas stations is 0.72 ($p$<0.01) (Figs. 2A, 2B), suggesting that both were controlled by the same air masse and climate. Local meteoric water line (LMWL) in the two monitoring sites are defined by: $\delta D_p = 6.91*\delta^{18}O_p + 3.02$ ($p$<0.01) for Le Mas and $\delta D_p = 7.08*\delta^{18}O_p + 5.03$ ($p$<0.01) for Villars based on the linear regression (Fig. 2C). In order to verify the reliability of LMWL equation, we also used other different methods, including ordinary least squares regression (OLSR) and precipitation weighted least squares regression (PWLSR) (Hughes and Crawford, 2012; Crawford et al., 2014). Whether weighted or non-weighted regression was considered, close slope and gradient values were observed from three methods (Table. 1). Rainfall stable isotopes are characterized by strong seasonal variations with depleted average values in winter months (December, January, February: -43.2‰ to -47.7‰ for $\delta D_p$ and -6.9‰ to -7.5‰ for $\delta^{18}O_p$) and enriched average values during summer months (June, July, August: -27.8‰ to -31.5‰ for $\delta D_p$ and -4.6‰ to -5.1‰ for $\delta^{18}O_p$) (Appendix Table 2) in Villars and Le Mas stations.

On a monthly timescale, $\delta^{18}O_p$ and local temperature show a positive correlation at Villars (R=0.61, $p$<0.0001) and Le Mas (R=0.62, $p$<0.0001) for the considered period (1996-2016) (Fig. 3A) with a T-$\delta^{18}O_p$ gradient of 0.17‰/°C and 0.15‰/°C

256 respectively. This indicates that the $\delta^{18}O_p$ in SW-France is mainly affected by local
257 temperature. Compared with observed (Fricke and O'Neill, 1999; Alley and Cuffey,
258 2001) and modelled (Jouzel et al., 1997; Schmidt et al., 2007) T-$\delta^{18}O_p$ gradient over
259 the global-scale, ranging from 0.17‰/°C to 0.9‰/°C, the T-$\delta^{18}O_p$ gradient in the Le
260 Mas and Villars stations are close to the lowest values. On the contrary, $\delta^{18}O_p$ and
261 local precipitation do not exhibit a significant correlation: R=0.19 at Le Mas and
262 R=0.29 at Villars, with a gradient of -0.7‰/100mm and -0.8‰/100mm, respectively
263 (Fig. 3B).

264 In order to assess local $\delta^{18}O_p$ records in SW-France whether or not can be
265 sensitive to regional parameters variations, correlations between $\delta^{18}O_p$ from Le Mas
266 and Villars stations and European temperatures with 5°x5° global grids were
267 calculated on the seasonal timescale for the 1996-2016 period. Results show that
268 significant correlations are mostly found for winter (DJF) and spring (MAM) (Figs.
269 4A, 4B, 4E, 4F). At Le Mas station, the time-series of $\delta^{18}O_p$ displays positive
270 correlation with Northern Europe temperatures and negative ones with the
271 temperature of South Europe and Mediterranean area (Fig. 4A). A similar pattern also
272 occurs for the Villars station, although these correlations are weaker (Fig. 4E)
273 possibly due to a lack of some monthly data in Villars (Fig. 4E; Appendix data).
274 Moreover, during spring (MAM), the correlation of $\delta^{18}O_p$ and regional temperature
275 shows positive (Northwest Europe) and negative (North Africa and Mediterranean
276 area) relationships at both stations (Figs. 4B and 4F). Unlike the high correlation

277 between local temperature and $\delta^{18}O_p$ on all months, this regional relationship is only
278 reflected in winter and spring (Fig. 3A and Fig. 4).

279 The relationship between regional precipitation and $\delta^{18}O_p$ for all the seasons was
280 also considered (Fig. 5). Despite the globally much weaker correlations, we observe
281 that, in winter, regional precipitation with 2.5°x 2.5° global grids and $\delta^{18}O_p$ shows a
282 similar spatial pattern between regional temperature and $\delta^{18}O_p$ (Figs. 4A, 4E, 5A, 5E).
283 During spring (MAM), the link between $\delta^{18}O_p$ and regional precipitation shows a
284 positive pattern with North Europe and North African and Mediterranean Sea and a
285 negative one all over the European continent (Figs. 5B and 5F). During summer (JJA)
286 and autumn (SON) seasons, no or less significant correlations were observed between
287 temperature/precipitation and $\delta^{18}O_p$ for both stations (Figs. 4C, 4D, 4G, 4H, 5C, 5D,
288 5G, 5H). The degrees of freedom corrections were calculated between the two 20-year
289 time-series of $\delta^{18}O_p$ from SW-France (Le Mas and Villars) and the Atlantic SST with
290 5°x5° global grids (Fig. 6). The results show that $\delta^{18}O_p$ values are positively
291 correlated with SST in the Gulf Stream of Mexico (Figs. 6B, 6F), and opposite to SST
292 in northern and southern of North Atlantic, inducing a tripolar SST distribution in the
293 North Atlantic in spring. However, during other seasons, no or less significant
294 correlations were observed between SST and $\delta^{18}O_p$ for both stations (Figs. 6A, 6C,
295 6D, 6E, 6G, 6H).

296 Note that whether we consider the pattern of $\delta^{18}O_p$ and European temperature or
297 precipitation in Le Mas and Villars stations in winter and spring, it is similar to the

298 spatial pattern between NAO phase and European temperature and precipitation
299 (Cassou et al., 2004; Baldini et al., 2008; Figs. 4A, 4E, 5A, 5E). The link between
300 NAO index and $\delta^{18}O_p$ seems to be confirmed by their high correlation ($p<0.01$ or
301 $p<0.05$) in winter ($R=0.45$ and $R=0.42$) and spring ($R=0.33$ and $R=0.36$) (Figs. 7A,7B,
302 7C, 7D).

303 **4.2 Relationship between $\delta^{18}O_p$ and initial moisture source on a**
304 **monthly timescale**

305 In order to localize the moisture sources of the rainfall (the percentage of initial
306 moisture, PIMS) that occur above Villars station, we first used the HYSPLIT software
307 for periods of high (summer) and low (winter) $\delta^{18}O_p$ (Fig. 8). Results show a clear
308 seasonal variability in the back trajectories with a much longer pathway in December,
309 January and February compared to the summer months (June, July and August) (Fig.
310 8). During winter, some vapor sources reach areas clearly beyond the 60° W meridian,
311 while in summer the extreme west source is significantly closer to Villars, around the
312 extreme east of Canada (Figs. 8D, 8E, 8F). But when replaced in the spatial pattern of
313 Figure 1, and looking at the actual percentages given by the software calculation
314 (Table 2), then it appears that water vapor source in winter is mostly distributed in the
315 region of NAGR (West North Atlantic: North America and Greenland) characterized
316 by a longer transportation (Table 2; Figs. 8A, 8B, 8C), while, in summer, it is mostly
317 from the closest source (PAWE: Proximal Atlantic and West Europe) (Table 2; Figs.
318 8D, 8E, 8F).

These results show that the sources (characterized by the PIMS) and rainfall $\delta^{18}O_p$ in SW-France are characterized by a well-marked seasonality: negative $\delta^{18}O_p$ excursions occur in winter when there is the longer initial moisture location (e.g. NAGR) (Table 2; Figs. 8A, 8B, 8C). On the contrary, the $\delta^{18}O_p$ in summer shows a positive $\delta^{18}O_p$ excursion, which coincides with the closer initial moisture location (e.g. PAWE) (Table 2; Figs. 8D, 8E, 8F).

During spring and autumn, there is no obvious contrasted PIMS (Fig. 9). We note however that PIMS in the near summer months (e.g. May and September) is derived from the increased closer moisture source (PAWE), and decreased longer moisture source (NAGR), corresponding to heavier values of $\delta^{18}O_p$ and $\delta D_p$ (Table 2 and Appendix Table 2; Figs. 9C, 9D). In contrast, in the near winter months (e.g. March and November), PIMS from the closer source (e.g. PAWE) is decreased, and longer sources is increased (e.g. NAGR) (Table 2; Figs. 9A, 9F), which indicates that the change of PIMS can regulate the $\delta^{18}O_p$ on the monthly timescale in SW-France.

These results highlight the close relationships between PIMS and $\delta^{18}O_p$ values at Villars (and Le Mas). A high PIMS from closer regions (e.g. PAWE and NA) is related to heavier $\delta^{18}O_p$ values while high PIMS from farther regions (e.g. NAGR) is related to lower $\delta^{18}O_p$ values (Table 2; Appendix Table 2). Linear equations have been established, for Le Mas and Villars stations, to quantify the relationship between $\delta^{18}O_p$ and PMIS (Table 3). Results show a positive relationship ($p<0.01$ or $p<0.05$) between $\delta^{18}O_p$ and PIMS in the region of PAWE and NA, and a negative relationship

($p$<0.01) between $\delta^{18}O_p$ and PIMS in the region of NAGR, whereas the rest of the regions (ME and DA) have much less impact on $\delta^{18}O_p$ values (Table 3).

## 4.3 Relationship between $\delta^{18}O_p$, d-excess and initial moisture source/local climate parameters on the annual and inter-annual timescale

On the annual timescale, a positive relationship ($p$<0.05), in both Le Mas and Villars stations, is observed between the annual average $\delta^{18}O_p$ ($\delta^{18}O_{ap}$) and annual mean temperature, with a T-$\delta^{18}O_{ap}$ gradient of 0.42‰/°C and 0.51‰/°C, respectively. These values fall in the range of gradients observed from global continental, marine and polar sites (0.17‰/°C to 0.9‰/°C; Clark and Fritz, 1999; Figs. 10A, 10B). At the opposite, P-$\delta^{18}O_{ap}$ gradients are low: -0.1‰/100mm and -0.07‰/100mm for Le Mas and Villars, and no significant correlation ($p$>0.1) was observed (Figs. 10C, 10D).

The locations of PIMS were determined using 5 days' reconstruction of air mass history during 1997-2016 (Table 4; Fig. 11). Curiously, the most distant areas (NAGR and PAWE) are the principal moisture sources (i.e., roughly >60%), while NA and DA are substantial contributors (i.e., roughly 34%), and the rest of the regions (ME and NESA) have little impact, at least for the 1997-2016 period (Table 4; Fig. 11). On the annual timescale, annual average values for $\delta^{18}O$ and $\delta D$ ($\delta^{18}O_{ap}$ and $\delta D_{ap}$) were calculated for the same period (Fig. 12A; Appendix Table 3). Annual $\delta^{18}O_{ap}$ value at Le Mas and Villars stations varies from -5.38 ‰ to -7.24 ‰ and -5.16 ‰ to -7.09 ‰, respectively (Appendix Table 3). The annual weighted $\delta^{18}O_p$ means ($\delta^{18}O_w$)

range from -4.63 ‰ to -7.00 ‰ and -4.69 ‰ to -6.79 ‰ for Le Mas and Villars respectively (Appendix Table 3). Whereas the $\delta^{18}O_p$ has a significant variation at the monthly timescale, it is much lower on the inter-annual timescale (Appendix Table 2, 3).

We also determine the correlation between PIMS and mean annual precipitation isotope composition ($\delta^{18}O_{ap}$ and $\delta^{18}O_w$) for the 1997-2016 period (Fig. 12; Table 4 and Appendix Table 2). Results show clear trends in the time-series of stable isotopes in Le Mas and Villars (Figs. 12A, 12B) : $\delta^{18}O_w$ and $\delta^{18}O_{ap}$ display a decreasing trend (for both stations Le Mas and Villars) on the 1997-2016 studied period, which coincides to **i)** a decreasing trend of the initial moisture source (PIMS) of closer regions (e.g., PAWE and NA) (Figs. 12C, 12D), and **ii)** to an increasing trend of PIMS of longer pathways (e.g., DA and NAGR) (Figs. 12E, 12F). However, weak or less inter-annual variations for local temperature and precipitation were observed over the past 20 year (Figs. 12G, 12H). In consequence, it appears that most of the inter-annual variability of rainfall isotopic composition ($\delta^{18}O_{p)}$ is controlled by the variation of the proportion of the different sources characterized by the PIMS trends.

The term of d-excess was firstly defined by Dansgaard (1964) as the following equation: d-excess= $\delta D-8*\delta^{18}O$, illustrating the degree of deviation from the equilibrium of isotopic fractionation caused by the kinetic fractionation in the evaporation of vapor (Dansgaard, 1964). Rainfall d-excess exhibited a weak inter-annual increasing trend in Villars and Le Mas over the past 20 year, and the

value range from 17.6 ‰ to -9.0 ‰ with the average value being 10.6 ‰ for Le Mas, and 17.6 ‰ to 1.7 ‰ with the average value being 9.5 ‰ for Villars, respectively (Figs. 13A, 13B), which is close to the value of 10 ‰ for the average of global precipitation. Annual variation of d-excess coincides to an increasing trend of PIMS of longer pathways (e.g., DA and NAGR) and a weak increasing trend in local temperature (Figs. 13A, 13B, 13C, 13D, 13E).

# 5. Discussions

## 5.1 Causes of the variations of precipitation isotope ($\delta^{18}O_p$, $\delta D_p$) in SW-France

Whether considering monthly or inter-annual timescale, it appears that $\delta^{18}O_p$ of both Le Mas and Villars stations follow variations of PIMS and local temperature. Several factors may be raised to explain the $\delta^{18}O_p$ variability: **i)** the length of the water vapor transport route which plays an important role on the Rayleigh fractionation process; **ii)** the initial mean seawater $\delta^{18}O$ ($\delta^{18}O_{sw}$) values which may be different; **iii)** the removal of moisture from an air mass which is temperature-dependent during Rayleigh fractionation, and the progressive condensation of the vapor requires the cooling of the air mass from the vapor of cloud to the falling rain (IAEA working group, 2000).

### 5.1.1 “amount effect” and “temperature effect” controls

Compared with global meteoric water line (GMWL: $\delta D=8\delta^{18}O+10$) (Craig, 1961; Dansgaard, 1964), we observed that there is a lower slope and a lower intercept in the LMWL of the two monitoring sites (Le Mas and Villars) (Fig. 2C) (Genty et al., 2014). This is a general case for continental stations (IAEA working group, 2000) and may be attributed to evaporation during the precipitation under the clouds and various complex phenomena linked to the history of rainfall (Dansgaard, 1964; Stewart, 1975; Gat, 1996; Peng et al., 2005; Yamanaka et al., 2007; Lachniet, 2009; Pang et al., 2011; Chen et al., 2015; Fig. 2C).

A positive correlation is observed between $\delta^{18}O_p$ and local monthly/annual mean temperature (Figs. 3A, 10A, 10B) in Le Mas and Villars. The main reason is that the air mass, after leaving from the moisture source, is dominated by Rayleigh fractionation processes, temperature and “rain-out” dependent (Dansgaard, 1954, 1964; Bowen, 2008). Water vapor in the atmosphere is difficult to isothermally condense, and any progress of atmospheric precipitation is caused by a temperature cooling (Dansgaard, 1954, 1964). When the condensed water is formed, then leaving water vapor immediately, the stable isotope ratio is depleted in the condensed water with the decrease of temperature (Dansgaard, 1964; Rozanki et al., 1993; Lachniet, 2009).

No significant correlation is observed between mean annual precipitation and $\delta^{18}O_p$, suggesting no “amount effect” at the Le Mas and Villars stations (Figs. 3B,

10C, 10D; Genty et al., 2014). Additionally, Keklec and Domínguez-Villar (2014) who conducted a monitoring of $\delta^{18}O_p$ in central Spain, proposed that all climate parameters with a seasonal cycle's characterization would exhibit a certain link with $\delta^{18}O_p$, however, when monitoring the relationship between single precipitation event with $\delta^{18}O_p$, these links are not visible (Keklec and Domínguez-Villar, 2014), further indicating that the amount of precipitation is not affecting the $\delta^{18}O_p$.

### 5.1.2 Moisture source effect

The transportation distance between moisture source and the monitoring site (latitude effect) has already shown an important control on the $\delta^{18}O_p$ (Aggarwal et al., 2004; Breitenbach et al., 2010; Chen and Li, 2018). Based on the Rayleigh fractionation process governing these links, the increased moisture transportation distances may result in depleted $\delta^{18}O_p$ value (Rindsberger et al., 1983; Field, 2010; Krklec and Domínguez-Villar, 2014; Krklec et al., 2018).

In winter months, the principal initial moisture sources derive from a longer source (NAGR) in comparison with the summer season characterized by a closer moisture source (PAWE) (Fig. 8). The precipitations that occur during the migration of moisture are enriched in $^{18}O$ leading to an impoverishment of remaining vapor and then resulting in a lower $\delta^{18}O_p$ (Araguás-Araguás et al., 2000; Breitenbach et al., 2010; Cai et al., 2016). Therefore, the longer the depression pathway, the lower $\delta^{18}O_p$ value (Araguás-Araguás et al., 2000; Lee & Fung, 2008; Risi et al., 2008; Lachniet et al.,

2009; Kurita, 2013; Cai et al., 2017). The mechanism is similar with "continental effect" where the rainout above the continent is the cause of impoverishment of the $\delta^{18}O$ with increasing distance from the ocean, but in fact very variable, i.e. from region to region and from season to season (IAEA working group, 2000).

Besides, the discrepancy of initial mean sea water $\delta^{18}O_{sw}$ values is also an important factor controlling the variation of $\delta^{18}O_p$ values in SW-France (Rozanski et al.,1993; Clark and Fritz, 1997; Cole et al., 1999; Friedman et al., 2002). Most of the moisture sources in Villars and Le Mas come from two main areas: NAGR in winter and PAWE in summer. Because the mean $\delta^{18}O_{sw}$ in the NAGR area (-4.0 ‰ to 0 ‰) (LeGrande and Schmidt, 2006) is lower than the one in the PAWE area (from 0 ‰ to 1.5 ‰) (LeGrande and Schmidt, 2006), it may also be a significant contribution to the observed $\delta^{18}O_p$ variation.

An important phenomenon appears at the inter-annual timescale where changes of the $\delta^{18}O_w$ and $\delta^{18}O_{ap}$ follow the inter-annual initial location of moisture source (Fig. 12), which is attributed to Rayleigh fractionation process and initial moisture sources (Figs. 11 and 12). Previous works have revealed that the $\delta^{18}O_d$ (drip-water $\delta^{18}O$) inherited the signal of atmospheric precipitation on the monthly timescales, and the influence of the "mixing effect" with "old water" in the epikarst zone (Pape et al., 2010; Li et al., 2011; Partin et al., 2013; Zhang & Li, 2019) seriously damp or even suppress the rainfall seasonal characteristics (e.g. heavier in summer and lighter in winter) (Genty et al., 2014), however, other studies indicated that the $\delta^{18}O_d$ and $\delta^{18}O_c$

462 can respond to the signal of $\delta^{18}O_w$ on the interannual timescale (Chen and Li, 2018;
463 Ellis et al., 2020). Our results show that the inter-annual $\delta^{18}O_p$ and $\delta D_p$ variations are
464 controlled by the mean annual change of the initial location of moisture source, which
465 provides new insights to explain climatic significance of oxygen isotope of drip water
466 and stalagmites on the interannual timescale in Villars Cave.

## 467 5.2 Variations of d-excess on the annual timescale

468 It is generally believed that d-excess is sensitive to moisture source conditions
469 (Pfahl and Wernli, 2008; Pfahl and Sodemann, 2014), therefore, which is suitable for
470 assessing the origin of water vapor. Moreover, some studies have proposed that high
471 and increasing d-excess values reflect fast evaporation (low RH) and stronger kinetic
472 isotope effects during evaporation (Clark and Fritz,1997; Dublyansky et al., 2018).

473 The linear variation of d-excess and PIMS of longer pathways (DA and
474 NAGR) exhibits an increasing trend in Le Mas and Villars (Figs. 13A, 13B, 13C,
475 13D), reflecting enhanced evaporations and stronger kinetic isotope effects in the
476 transportation of vapor while moisture from longer pathways was increased over the
477 entire period of observation (Clark and Fritz, 1997; Pfahl and Wernli, 2008;
478 Dublyansky et al., 2018). The increase of air temperature at the monitoring stations
479 over the past 20 years leads to the enhancement of water vapor evaporation, inducing
480 the rising change of precipitation d-excess (Figs. 13A, 13B, 13E). Hence, our results
481 suggest that the d-excess variations in paleo-record (e.g. ice cores) should be adapted

to reflect moisture source characterized by atmospheric circulation and local temperature.

## 5.3 Links between NAO and $\delta^{18}O_p$ in SW-France

During a positive phase of the NAO, a large pressure gradient between the Azores (High Pressure) and Iceland (Low Pressure) across the North Atlantic creates higher winter temperatures and precipitation over the Atlantic and Northern Europe while it is lower over Mediterranean Sea and North Africa (Hurrell, 1995, 1996; Uvo, 2003). The exactly opposite pattern in negative NAO phase is found when the pressure gradient between Azores and Iceland decreases by shifting southwards the northern hemisphere westerly jet-stream (Hurrell, 1995).

NAO in different phase plays an important role in the length of water vapor transport in winter and spring (Baldini et al., 2008). When winter and spring NAO index is in positive excursion, warmer westerly winds will carry 18O moisture with shorter transportation distance, resulting in heavier $\delta^{18}O_p$ values in SW-France (Baldini et al., 2008; Langebroek et al., 2011), therefore NAO index and $\delta^{18}O_p$ exhibit a positive correlation (Fig. 7A, 7B, 7C, 7D). However, NAO only take a strengthened or weakened effect on the length of water vapor transport in winter (Baldini et al., 2008), which will not change the fact that most of winter moisture source distributed in the region of longer distance (West North Atlantic: North America and Greenland) (Section 4.2; Krklec and Domínguez-Villar, 2014). The isotopic time series at the

seasonal timescales show correlations with NAO index, providing a useful NAO proxy ($\delta^{18}O_p$) to indicate the variation in seasonal paleo-NAO index. However, when it comes to the relationship between NAO and $\delta^{18}O_p$ in the inter-annual timescale, a particularly weak correlation ($p>0.1$) was found.

## 5.4 Quantifying the relationship between PIMS/temperature and $\delta^{18}O_p$ in SW-France

The variations of PIMS and local temperature have been identified as important contributors for the observed $\delta^{18}O_p$ changes in SW-France. Therefore, combining the links between PIMS/temperature and $\delta^{18}O_p$, several equations were established using multiple linear regression analysis methods as followed:

EQ (1) for Le Mas station:

$$\delta^{18}O_p=0.038*PAWE+0.046*NA+0.054*ME+0.02*DA+0.025*NAGR+0.119*T-10.929,$$

$R=0.965$, $p<0.01$

Where $\delta^{18}O_p$ indicates precipitation $\delta^{18}O$ (V-SMOW), and T (°C) indicate the local monthly temperature in Le Mas.

EQ (2) for Villars station:

$$\delta^{18}O_p= 0.035*PAWE+0.031*NA+0.054*ME-0.001*DA+0.005*NAGR+0.049*T-8.637,$$

$R=0.942$, $p<0.05$

Where $\delta^{18}O_p$ indicates precipitation $\delta^{18}O$ (V-SMOW), and T (°C) indicate the local monthly temperature in Villars.

These two equations allow to evaluate the importance of the factors (PIMS, Temperature) variability on the $\delta^{18}O_p$ variability. Results show that the following factors influence the $\delta^{18}O_p$ in the order on importance: Temperature>NAGR > PAWE>NA>DA>ME at the monthly timescale. We use the SPSS software to calculate the variance of contribution rate, and the proportion in the four main principal components are 60.6% (Temperature), 16.6% (NAGR), 15.4% (PAWE), 6.2% (NA), the rest of two-component (DA and ME) is <2%. Therefore, in any case, considering the range of variability of various contributions from different moisture source regions and local temperature, it is obviously found that local temperature is the principal variable controlling the oxygen isotope composition of precipitation in the continental European at a monthly timescale. In addition, adding the different variable step by step and look at the results after each step, we could we found that multiple linear regression is more accurate to describe the relationship between isotopes and water vapor sources and air temperature compared to linear regression methods (Appendix Table 4).

The use of HYSPLIT model for tracking moisture source is providing a good example for how to accurately calculate the relationship between $\delta^{18}O_p$ and moisture sources. Different from regional/general circulation models of the $\delta^{18}O_p$ (Cruz- San Julián et al., 1992; Celle-Jeanton et al., 2001; Sodemann et al., 2008; Baldini et al., 2010; Gao et al., 2011; Bershaw et al., 2012), this study not only provides the quantified mathematical equations based among the longest isotopic isotope time

543 series and the variations of PIMS (over 20 years), but also determines the extent of the
544 impact on the monthly timescale.

545 Additionally, the speleothem $\delta^{18}O$ in the Villars Cave, also recorded a series of
546 abrupt climatic events on the centennial-millennial timescales, such as
547 Dansgaard-Oeschger, Heinrich and 8.2 ka events (Genty et al., 2001, 2003, 2006;
548 Genty, 2008; Wainer et al., 2009, 2010, 2013; Genty et al., 2014). In this study, the
549 long monitoring-based work established a link between local climate parameters and
550 the $\delta^{18}O_p$, which can be used for interpreting the significance of speleothem $\delta^{18}O$. No
551 or less correlation was observed between the $\delta^{18}O_p$ and local precipitation, indicating
552 that speleothem $\delta^{18}O$ in Villars Cave likely cannot reconstruct local precipitation. In
553 contrast, change in $\delta^{18}O_p$ can be linked to both the change of moisture source and to
554 the local temperature variation.

555 ## 6. Conclusions

556 Based on the observations and models on $\delta^{18}O_p$ and $\delta D_p$, moisture source, and
557 regional/local climate parameters during the 1997-2016 period at the Le Mas and
558 Villars meteorological stations, SW-France, the following conclusions can be drawn:

559 **(1)** Based on HYSPLIT model, we have quantified the percentage of initial moisture
560 source (PIMS) for different months and found shorter transportation distances during
561 summer months and longer ones during winter, which is consistent with the observed
562 seasonal variations of $\delta^{18}O_p$.

**(2)** The variation of temperature and PIMS are important factors that are the main causes on the seasonal variation of the $\delta^{18}O_p$. In the order of importance, the following factors influence the $\delta^{18}O_p$: Temperature>NAGR>PAWE>NA>DA>ME, and the proportion of the four main principal components are 60.6% (Temperature), 16.6% (NAGR), 15.4% (PAWE), 6.2% (NA) on the monthly timescale.

**(3)** On the annual timescale, $\delta^{18}O_p$ maintains a positive relationship with local mean annual temperature, however no evidences for its "amount effect" has been observed.

**(4)** On a longer timescale, an important result shows that an inter-annual decreasing trend was observed for the $\delta^{18}O_p$ ($\delta^{18}O_{ap}$ and $\delta^{18}O_w$), following the variation of annual PIMS. We observed, over the past 20 years, that the percentage of a farther moisture source region (NAGR) was increased, at the opposite, there is a decreasing trend for the closer source (PAWE).

**(5)** The linear variation trend over the past 20 years of d-excess coincides to the variations of PIMS in longer pathways (DA and NAGR) and local temperature on the inter-annual timescale, which is likely due to the global temperature increase and the change of moisture source characterized by atmospheric circulation in SW-France.

**(6)** The variation of moisture distribution regions should be considered when interpreting the climatic significance for speleothem oxygen isotopic records in SW-France.

## Acknowledgments

The long monitoring study on Villars Cave was possible thanks to the constant help of the Versaveau family, who have always shown interest in our research. Similarly, Le Mas station rainfall sampling was able to the support of the Genty family during all along these years. We would like to express sincere thanks to Xi Lei for her help in the drawings and Dr. Zhaojun Zhan (school of geography and ocean, Nanjing University, China) for her useful discussions. This research was supported by the China Scholarship Council (CSC) to Jian. Zhang (201906990014). This long monitoring work has been funded, since 1996, by several programs from the CNRS (INSU), and three laboratories (GEOPS, Orsay, Paris-Saclay University; Laboratoire des Sciences du Climat et de l'Environnement, LSCE, CEA/CNRS/UVSQ and Environnements et Paléoenvironnements Océaniques et Continentaux, EPOC, Bordeaux University, France). Le Mas and Villars stations are part of the new French rainfall isotopic network RENOIR SOERE Observatory of the INSU/CNRS.

## Competing financial interests

The authors declare no competing financial interests.

## References

Abouelmagd, A., Sultan, M., Milewski, A., Kehew, A.E., Sturchio, N.C., Soliman, F., Krishnamurthy, R.V., Curtim, E., 2012. Towards a better understanding of palaeoclimatic regimes that recharged the fossil aquifers in North Africa: Inferences from stable isotope and remote sensing data. Palaeogeogr., Palaeoclim., Palaeoecol. 329-330, 137–149.

603 Aggarwal, P.K., Frohlich, K., Kulkarni, K.M., Gourcy, L.L., 2004. Stable isotope evidence for
604 moisture sources in the Asian summer monsoon under present and past climate regimes.
605 Geophy. Res. Let. 31(8).

606 Allen, S. T., Kirchner, J. W., & Goldsmith, G. R. (2018). Predicting spatial patterns in
607 precipitation isotope ($\delta^2H$ and $\delta^{18}O$) seasonality using sinusoidal isoscapes. Geophysical
608 Research Letters, 45, 4859– 4868. https://doi.org/10.1029/2018GL077458.

609 Alley, R.B., Cuffey, K.M., 2001. Oxygen- and hydrogen-isotopic ratios of water in precipitation:
610 beyond paleothermometry. Rev. Mineral. Geochem. 43, 527–553.

611 Araguás-Araguás, L. J., and M. F. Diaz Teijeiro. 2005.Isotope composition of precipitation and
612 water vapour in the Iberian Peninsula: first results of the Spanish network of isotopes in
613 precipitation. At. Energy. Agency. Tech. Report 1453: 173-190.

614 Araguás-Araguás, L., Froehlich, K., Rozanski, K., 2000. Deuterium and oxygen-18 isotope
615 composition of precipitation and atmospheric moisture. Hydro. process, 14(8), 1341–1355.

616 Baldini, L.M., McDermott, F., Foley, A.M., Baldini, J.U.L., 2008. Spatial variability in the
617 European winter precipitation $\delta^{18}O$-NAO relationship: Implications for reconstructing
618 NAO-mode climate variability in the Holocene. Geophys. Res. Lett. 35(4), L04709.

619 Breitenbach, S.F.M. et al. Breitenbach, S. F., Adkins, J. F., Meyer, H., Marwan, N., Kumar, K. K.,
620 Haug, G. H., 2010. Strong influence of water vapor source dynamics on stable isotopes in
621 precipitation observed in Southern Meghalaya, NE India. Earth Planet. Sci. Lett. 292(1-2):0–
622 220.

623 Bowen, G.J., 2008. Spatial analysis of the intra-annual variation of precipitation isotope ratios and
624 its climatological corollaries. J. Geophys. Res. Atmos.113.

625 Cassou, C., Terray, L., Hurrell, J. W., Deser, C., 2004. North Atlantic winter climate regimes:
626 Spatial asymmetry, stationarity with time, and oceanic forcing. J. Clim. 17(5), 1055–1068.

627 Cai, Z., Tian. L., Bowen, G. J., 2017. ENSO variability reflected in precipitation oxygen isotopes

628 across the Asian Summer Monsoon region. Earth Planet. Sci. Lett. 475:25–33.

629 Celle-Jeanton H., Travi Y. and Blavoux B., 2001. Isotopic typology of the precipitation in the
630 western Mediterranean region at three different timescales. Geophys. Res. Lett. 28(7), 1215–
631 1218.

632 Chen, B., A. F. Stein, N. Castell, J. D. de la Rosa, A. M.Sanchez de la Campa, Y.
633 Gonzalez-Castanedo., R. R. Draxler., 2012., Modeling and surface observations of arsenic
634 dispersion from a large Cu-smelter in southwestern Europe. Atmos. Environ., 49, 114–122.

635 Chen, C-J., Li, T-Y. 2018. Geochemical characteristics of cave drip water respond to ENSO based
636 on a 6-year monitoring work in Yangkou cave, Southwest China, J. Hydrol, 561:896–907.

637 Chen, F. L., Zhang, M. J., Wang, S. J., Ma, Q., Zhu, X. F., Dong, L., 2015. Relationship between
638 sub-cloud secondary evaporation and stable isotopes in precipitation of Lanzhou and
639 surrounding area, Quatern. Int., 380-381, 68–74.

640 Clark, I., Fritz, P., 1997.Environmental Isotopes in Hydrology. LewisPublishers, NewYork.

641 Cole, J.E., Rind, D., Webb, R.S., Jouzel, J., Healy, R., 1999. Climatic controls on interannual
642 variability of precipitation $\delta^{18}O$: Simulated influence of temperature, precipitation amount, and
643 vapor source region. J. Geophys. Res., 104, 14223–14235.

644 Craig, H., 1961. Isotopic variations in meteoric waters. Science. 133(3465): 1702–1703.

645 Craig, H., Gordon, L.I., 1965. Deuterium and oxygen 18 variations in the ocean and the marine
646 atmosphere, The stable isotopes in oceanographic studies and paleotemperatures, Lab. Geol.
647 Nucl., Pisa, Italy, 9–130.

648 Crawford, J., Hughes, C. E., Lykoudis, S. 2014. Alternative least squares methods for determining
649 the meteoric water line, demonstrated using GNIP data. J. Hydrol, 519, 2331-2340.

650 Cruz-San Julian, J. L. Araguas, K. Rozanski, J. Benavente, J. Cardenal, M. C. Hidalgo, S.
651 Garcia-Lopez, J. C. Martinez-Garrido, F. Moral & M. Olias., 1992. Sources of precipitation
652 over South-Eastern Spain and groundwater recharge. An isotopic study, Tellus B: Chemical

653 and Physical Meteorology, 44:3, 226–236.

654 Dansgaard, W., 1954. The $O^{18}$-abundance in fresh water. Geochim.Cosmochim. Acta. 6, 241–260.

655 Dansgaard, W., 1964. Stable isotopes in precipitation. Tellus 16, 436–468.

656 Draxler, R. R., Hess, G. D., 1998. An overview of the HYSPLIT_4 modelling system for
657 trajectories, dispersion and deposition. Aust. Meteorol. Mag. 47(4), 295–308.

658 Draxler, R. R., and G. D. Rolph., 2010. HYSPLIT (HYbrid Single-Particle Lagrangian Integrated
659 Trajectory) model access via NOAA ARL READY website (http://ready. arl. noaa.
660 gov/HYSPLIT. php). NOAA Air Resources Laboratory. Silver Spring, MD, 25.

661 Duffourg, F., Ducrocq, V., 2011. Origin of the moisture feeding the Heavy Precipitating Systems
662 over Southeastern France. Nat. Hazard. Earth. Sys. 11(4), 1163.

663 Dumitru, O.A., Forray, F.L., Fornós, J.J., Ersek, V., Onac, B.P., 2017. Water isotopic variability in
664 Mallorca: a path to understanding past changes in hydroclimate. Hydrol. Process. 31, 1, 104–
665 116.

666 Dublyansky, Y. V., Klimchouk, A. B., Tokarev, S. V., Amelichev, G. N., Langhamer, L., Spötl, C.
667 2018. Stable isotopic composition of atmospheric precipitation on the Crimean Peninsula and
668 its controlling factors. J. Hydrol, 565, 61-73.

669 Ellis, S. A, Cobb, K. M., Moerman, J. W., Partin, J. W., Bennett, A. L., Malang, J., Gerstner,H.,
670 Tuen, A.A., Extended cave drip water time series captures the 2015–2016 El Niño in Northern
671 Borneo. Geophys. Res. Lett., 2020, 47(5).

672 Field, R.D., 2010. Observed and modeled controls on precipitation $\delta^{18}O$ over Europe: From local
673 temperature to the Northern Annular Mode, J. Geophys. Res. 115, D12101.

674 Fischer, M. J., D. Mattey., 2012. Climate variability and precipitation isotope relationships in the
675 Mediterranean region. J. Geophys. Res. Atmos.117.D20.

676 Fricke H. C., O'Neil J. R., 1999. The correlation between $^{18}O/^{16}O$ ratios of meteoric water and

677 surface temperature: its use in investigating terrestrial climate change over geologic time.
678 Earth Planet. Sci. Lett. 170, 181–196.

679 Friedman, I., Harris, J.M., Smith, G.I., Johnson, C.A., 2002. Stable isotope composition of waters
680 in the Great Basin, United States, 1, Air-mass trajectories, J. Geophys. Res. 107(D19), 4400.

681 Gat, J.R., 1996. Oxygen and hydrogen isotopes in the hydrologic cycle. Annu. Rev. Earth. Planet.
682 Sci.24, 225–262.

683 Gat. J. R., 2010. Isotope Hydrology: A Study of the Water Cycle. Imperial College Press, London.

684 Genty. D., Baker. A., Massault. M., Proctor. C., Gilmour. M., PonsBranchu. E., Hamelin B., 2001.
685 Dead carbon in stalagmites: carbonate bedrock paleodissolution vs. ageing of soil organic
686 matter. Implication for $^{13}C$ variation in speleothems. Geochim.Cosmochim. Acta 65, 3443–
687 3457.

688 Genty, D., Blamart, D., Ouahdi, R., Gilmour, M., Baker, A., Jouzel, J., & Van-Exter, S. 2003.
689 Precise dating of Dansgaard–Oeschger climate oscillations in western Europe from stalagmite
690 data. Nature, 421(6925), 833.

691 Genty. D., Blamart. D., Ghaleb. B., Plagnes. V., Causse. C., Bakalowicz. M., Zouari. K., Chkir.N.,
692 Hellstrom. J., Wainer. K., Bourges. F., 2006. Timing and dynamics of the last deglaciation
693 from European and North African delta C-13 stalagmite profiles – comparison with Chinese
694 and South Hemisphere stalagmites. Quatern. Sci. Rev. 25, 2118–2142.

695 Genty. D., 2008. Palaeoclimate research in Villars Cave (Dordogne, SW-France). Int. J. Speleol.
696 37, 173–191.

697 Genty, D., Labuhn, I., Hoffmann, G., Danis, P.A., Mestre, O., Bourges, F., Wainer, K., Massault,
698 M., Van Exter, S., Régnier, E., Orengo, Ph., Falourd, S., Minster, B., 2014. Rainfall and cave
699 water isotopic relationships in two South-France sites. Geochim. Cosmochim. Acta. 131 (5),
700 323–343.

701 Giuntoli, I., Renard, B., Vidal, J. P., Bard, A., 2013, Low flows in France and their relationship to

large-scale climate indices. J. Hydrol, 482: 105-118.

Hoffmann, G., Werner, M., Heimann, M., 1998. The Water isotope module of the ECHAM atmospheric general circulation model - A study on time scales from days to several years. J. Geophys. Res. 103, 16,871–16,896.

Hu, C.Y. et al., 2008. Quantification of Holocene Asian monsoon rainfall from spatially separated cave records. Earth Planet. Sci. Lett. 266(3):221–232.

Hughes, C. E., Crawford, J. 2012. A new precipitation weighted method for determining the meteoric water line for hydrological applications demonstrated using Australian and global GNIP data. J. Hydrol. 464, 344-351.

Hurrell, J.W., 1995. Decadal trends in the north Atlantic oscillation: regional temperatures and precipitation, Science, 269, 676-679.

Hurrell, J. W., 1996, Influence of variations in extratropical wintertime teleconnections on Northern Hemisphere temperature, Geophys. Res. Lett., 23, 665- 668.

IAEA Publish chapter 4. 2000. Environmental isotopes in the hydrological cycle. 39.

Krklec, K., Domínguez-Villar, D., Lojen, S., 2018. The impact of moisture sources on the oxygen isotope composition of precipitation at a continental site in central Europe, J. Hydrol., 561, 810–821.

Krklec. Kristina., David. Domínguez-Villar., 2014. Quantification of the impact of moisture source regions on the oxygen isotope composition of precipitation over Eagle Cave, central Spain. Geochim. Cosmochim. Acta. 134: 39–54.

Kurita, N. 2013. Water isotopic variability in response to meso-scale convective system over the tropical ocean. J. Geophys. Res. Atmos., 118, 10 376–10 390.

Lachniet. M. S., 2009. Climatic and environmental controls on speleothem oxygen-isotope values. Quatern. Sci. Rev. 28, 412–432.

Ladouche. Bernard., Aquilina. Luc., Dörfliger. Nathalie., 2009. Chemical and isotopic

727 investigation of rainwater in Southern France (1996–2002): Potential use as input signal for
728 karst functioning investigation. J. Hydro. 367.1-2: 150–164.

729 Langebroek, P.M., Werner, M., Lohmann, G., 2011. Climate information imprinted in
730 oxygen-isotopic composition of precipitation in Europe. Earth Planet. Sci. Lett. 311(1–2):144–
731 154.

732 Lee, J.-E., Fung, I., 2008. ‘‘Amount effect’’ of water isotopes and quantitative analysis of
733 post-condensation processes. Hydrol. Processes, 22, 1–8, doi:10.1002/hyp.6637.

734 LeGrande, A.N., Schmidt, G.A., 2006. Global gridded data set of the oxygen isotopic composition
735 in seawater. Geophy. Res. Let.33.

736 Li, T.-Y., Shen, C.-C., Li, H.-C., Li, J.-Y., Chiang, H.-W., Song, S.-R., Yuan, D.-X., Lin, C.D.J.,
737 Gao, P., Zhou, L.-P., Wang, J.-L., Ye, M.-Y., Tang, L.-L., Xie, S.-Y., 2011. Oxygen and
738 carbon isotopic systematics of aragonite speleothems and water in Furong Cave, Chongqing,
739 China. Geochim. Cosmochim. Acta. 75(15), 4140-4156.

740 McDermott, F., Atkinson, T. C., Fairchild, I. J., Baldini, L. M., Mattey, D. P., 2011. A first
741 evaluation of the spatial gradients in delta (18)O recorded by European Holocene speleothems.
742 Global Planet. Change 79, 275–287.

743 McCarthy, G. D., Haigh, I. D., Hirschi, J. J. M., Grist, J. P., Smeed, D. A. 2015. Ocean impact on
744 decadal Atlantic climate variability revealed by sea-level observations. Nature, 521(7553),
745 508-510.

746 Numaguti, A., 1999. Origin and recycling processes of precipitating water over the Eurasian
747 continent: Experiments using an atmospheric general circulation model. J. Geophys. Res.
748 Atmos. 104, 1957–1972.

749 O'Reilly, C. H., Huber, M., Woollings, T., Zanna, L. 2016. The signature of low-frequency
750 oceanic forcing in the Atlantic Multidecadal Oscillation. Geophy. Res. Let, 43(6), 2810-2818.

751 Pang, Z. H., Kong, Y. L., Froehlich, K., Huang, T. M., Yuan, L. J., Li, Z. Q., Wang, F. T., 2011.

752 Processes affecting isotopes in precipitation of an arid region, Tellus. B., 63, 352–359.

753 Pape, J. R., Banner, J. L., Mack, L. E., Musgrove, M., Guilfoyle, A., 2010. Controls on oxygen
754 isotope variability in precipitation and cave drip waters, central Texas, USA. J.
755 Hydrol, 385(1-4), 203–215.

756 Partin, J. W. Cobb, K. M., Adkins, J. F., Tuen, A. A., Clark, B. 2013. Trace metal and carbon
757 isotopic variations in cave drip water and stalagmite geochemistry from northern Borneo.
758 Geochem. Geophys. Geosyst. 14(9):3567–3585.

759 Peng, H., Mayer, B., Norman, A. L., Krouse, H. R., 2005. Modelling of hydrogen and oxygen
760 isotope compositions for local precipitation. Tellus B. 57(4), 273–282.

761 Petit, J.R., Jouzel, J., Raynaud, D., Barkov, N.I., Barnola, J.-M., Basile, I.,Bender, M., Chappellaz,
762 J., Davis, M., Delaygue, G., Delmotte, M., Kotlyakov, V.M., Legrand, M., Lipenkov, V.Y.,
763 Lorius, C., Pepin, L., Ritz, C., Saltzman, E., Stievenard, M., 1999. Climate and atmospheric
764 history of the past 420,000 years from the Vostok ice core, Antarctica. Nature 399, 429–436.

765 Pfahl, S. and Sodemann, H., 2014. What controls deuterium excess in global precipitation?
766 Climate of the Past, 10(2), pp.771-781.

767 Pfahl, S., Wernli, H., 2008. Air parcel trajectory analysis of stable isotopes in water vapor in the
768 eastern Mediterranean. J. Geophys. Res. 113: D20104.

769 Risi. C., Bony. S., Vimeaux. F., 2008. Influence of convective processes on the isotopic
770 composition ($\delta^{18}O$ and $\delta D$) of precipitation and water vapour in the tropics: 2 Physical
771 interpretation of the amount effect. J. Geophys. Res. 113, D19306.

772 Rolph, G. D., Coauthors, 2009. Description and verification of the NOAA Smoke Forecasting
773 System: The 2007 fire season. Wea. Forecasting, 24, 361–378.

774 Rozanski, K., Araguás-Araguás, L., Gonfiantini, R., 1993. Isotopic patterns in modern global
775 precipitation. In: Swart, P.K., Lohmann, K.L., McKenzie, J., Savin, S. (Eds.), Climate Change
776 in Continental Isotopic Records. American Geophysical Union, Washington, DC, pp. 1–37.

Sánchez‐Murillo, R., Esquivel‐Hernández, G., Corrales‐Salazar, J. L., Castro‐Chacón, L., Durán‐Quesada, A. M., Guerrero‐Hernández, M., Delgado,V., Barberena, J., Montenegro-Rayo. K., Calderón. Heyddy., Chevez.C., Peña-Paz. T., García-Santos, Saúl., Ortiz-Roque, Pedro., Alvarado-Callejas, Y., Benegas.L., Hernández-Antonio, A., Matamoros-Ortega, M., Ortega,L Terzer-Wassmuth,S Chevez, C. (2020). Tracer hydrology of the data‐scarce and heterogeneous Central American Isthmus. Hydrological Processes. 2020;1–16

Schmidt, G.A., LeGrande, A.N., Hoffmann, G., 2007. Water isotope expressions of intrinsic and forced variability in a coupled ocean-atmosphere model, J. Geophys. Res. 112, D10103.

Sharp, Z., 2007. Principles of Stable Isotope Geochemistry. Pearson Prentice Hall, Upper Saddle River, NJ.

Sodemann, H., Schwierz, C., Wernli, H., 2008. Interannual variability of Greenland winter precipitation sources: Lagrangian moisture diagnostic and North Atlantic Oscillation influence. J. Geophys. Res. 113, D03107.

Stein, A.F., Draxler, R.R., Rolph, G.D., Stunder, B.J.B., Cohen, M.D., Ngan, F., 2015. NOAA's HYSPLIT atmospheric transport and dispersion modeling system, Bull. Amer. Meteor. Soc., 96, 2059–2077.

Stewart, M. K.1975. Stable isotope fractionation due to evaporation and isotopic exchange of falling waterdrops: Applications to atmospheric processes and evaporation of lakes, J. Geophys. Res., 80, 1133-1146.

Sturm, K., Hoffmann, G., Langmann, B., Stichler, W., 2005. Simulation of $^{18}O$ in precipitation by the regional circulation model REMOiso. Hydrol. Process. 19, 3425–3444.

Tang, Y., Pang, H., Zhang, W., Li, Y., Wu, S., Hou, S., 2015. Effects of changes in moisture source and the upstream rainout on stable isotopes in summer precipitation – a case study in Nanjing, East China, Hydrol. Earth. Syst. Sc., 12, 3919–3944.

Uemura, R., Masson-Delmotte, V., Jouzel, J., Landais, A., Motoyama, H., Stenni, B., 2012.

Ranges of moisture-source temperature estimated from Antarctic ice cores stable isotope records over glacial-interglacial cycles, Clim. Past, 8, 1109–1125.

Vo, C. B., 2003, Analysis and regionalization of Northern European winter precipitation based on its relationship with the North Atlantic Oscillation, Int. J. Climatol., 23, 1185-1194.

Wang, Y.J., Cheng, H., Edwards, R.L., An, Z.S., Wu, J.Y., Shen, C.C., Dorale, J.A., 2001.A high-resolution absolute-dated Late Pleistocene monsoon record from Hulu Cave, China. Science. 294, 2345–2348.

Wainer K., Genty D., Blamart D., Hofmann D., Couchoud I., 2009, A new stage 3 millennial climatic variability record from a SW France speleothem, Palaeogeogr., Palaeoclim., Palaeoecol., 271: 130-139.

Wainer K., Genty D., Blamart D., Daëron M., Bar-Matthews M., Vonhof H., Dublyansky Y., Pons-Branchu E., Thomas L., van Calsteren P., Quinif Y. and Caillon N., 2011, Speleothem record of the last 180 ka in Villars cave (SW France):Investigation of a large d18O shift between MIS6 and MIS5, Quatern. Sci. Rev., 30:130-146.

Wainer K., Genty D., Blamart D., Bar-Matthews M., Quinif Y., Plagnes V., 2013, Millennial climatic instability during penultimate glacial period recorded in a south-western France speleothem., Palaeogeogr., Palaeoclim., Palaeoecol., 376:122-131.

Yamanaka, T., Tsujimura, M., Oyunbaatar, D., Davaa, G., 2007. Isotopic variation of precipitation over eastern Mongolia and its implication for the atmospheric water cycle, J. Hydrol., 333, 21–34.

Zhang, J., Li. Ting-Yong., 2019. Seasonal and inter-annual variation of hydro-chemical characteristics and stable isotopic compositions of drip waters in Furong Cave, Southwest China based on 12 years' monitoring. J. Hydrol. 572:40-50.

Zhang, P.Z., Cheng, H., Edwards, R.L., Chen, F.H., Wang, Y.J., Yang, X.L., Liu, J., Tan, M., Wang, X.F., Liu, J.H., An, C.L., Dai, Z.B., Zhou, J., Zhang, D.Z., Jia, J.H., Jin, L.Y., Johnson, K.R., 2008. A test of climate, sun and culture relationship from an 1810-year Chinese cave

record. Science 322, 940–942.

## Caption

**Figure 1** Location of the two monitoring stations. **(A)** Location of the study area, including Villars (a, blue point) and Le Mas (b, red point) in SW-France. The range of initial $\delta^{18}O_{sw}$ value is from 0 to 1.5 ‰ in PAWE (see Appendix Table 1 for areas names), 0.5 to 2.0 ‰ in DA, 0 to 0.5 ‰ in NA, -4.0 to 0 ‰ in NAGR, 1.5 to 2.5 ‰ in ME, and 0 to1.0 ‰ in NENA (referred and modified from Lachniet, 2009; Krklec and Domínguez-Villar, 2014). **(B)** Geomorphologic map and site distribution for the surrounding of the Villars and Le Mas stations. The arrow indicates the direction of the initial moisture source.

**Figure 2** Time series of monthly rainfall $\delta^{18}O_p$ at Villars **(A)** and Le Mas **(B)** monitoring stations. **(C)** Local meteoric water line (LMWL) for Le Mas (red), and Villars (blue) based on the linear regression. The Global Meteoric Water Line (GMWL) in green (Craig, 1961) is plotted for comparison.

**Figure 3 (A)** Correlation between rainfall $\delta^{18}O_p$ and local monthly temperature for the 1997-2016 period. **(B)** Correlation between rainfall $\delta^{18}O_p$ and local monthly precipitation for the 1997-2016 period.

**Figure 4** Seasonal correlation maps between $\delta^{18}O_p$ from Le Mas (top panel) and Villars (bottom panel) and temperatures over Europe during the period of 1997-2016 (Some disconnected data is not considered). **(A, E)** DJF, **(B, F)** MMA, **(C, G)** JJA, **(D,**

**H)** SON. Black crosses indicate grid points where the correlation is not significant at the 90% confidence level. However, the discontinuities of $\delta^{18}O_p$ data was excluded in some years (Appendix data). The figure was produced using the programming language R. The degrees of freedom corrections were calculated by timeseries autocorrelations (McCarthy et al., 2015).

**Figure 5** Seasonal correlation maps between $\delta^{18}O_p$ from Le Mas (top panel) and Villars (bottom panel) and precipitation over Europe during the period of 1997-2016 (Some disconnected data is not considered). **(A, E)** DJF, **(B, F)** MMA, **(C, G)** JJA, **(D, H)** SON. Black crosses indicate grid points where the correlation is not significant at the 90% confidence level. However, the discontinuities of $\delta^{18}O_p$ data was excluded in some years (Appendix data). The figure was produced using the programming language R. The degrees of freedom corrections were calculated by timeseries autocorrelations (McCarthy et al., 2015).

**Figure 6** Seasonal correlation maps between $\delta^{18}O_p$ from Le Mas (top panel) and Villars (bottom panel) stations and SST in North Atlantic during the 1997-2016 period (Some disconnected data is not considered). **(A, E)** DJF, **(B, F)** MMA, **(C, G)** JJA, **(D, H)** SON. Black crosses indicate grid points where the correlation is not significant at the 90% confidence level. However, the discontinuities of $\delta^{18}O_p$ data was excluded in some years (Appendix data). The figure was produced using R programming language. The degrees of freedom corrections were calculated by timeseries autocorrelations (McCarthy et al., 2015).

**Figure 7 (A)** Correlation between $\delta^{18}O_p$ and NAO index at Le Mas during the winter period of 1997-2016. **(B)** Correlation between $\delta^{18}O_p$ and NAO index at Villars during the winter period of 1997-2016. **(C)** Correlation between $\delta^{18}O_p$ and NAO index at Le Mas during the spring period of 1997-2016. **(D)** Correlation between $\delta^{18}O_p$ and NAO index at Villars during the winter period of 1997-2016.

**Figure 8** Back trajectories for contrasted seasons, winter (December **(A)**, January **(B)**, February **(C))** and summer **(**June **(D)**, July **(E)**, August **(F))**. The star indicates the location of Villars, and the detailed data of PIMS is listed in Table 2. The air mass history was calculated at 1500 m a.g.l over the past 120 hours, and every 6 hours outputted a trajectory, then we integrated all of the calculated data into ten trajectories. The back trajectories are presented for monthly variations for the period of 1997-2016.

**Figure 9** Back trajectories for March **(A)**, April **(B)**, May **(C)**, September **(D)**, October **(E)** and November **(F)**. The star indicates the location of Villars, and the detailed data of moisture source is listed in Table 1. The air mass history was calculated at 1500 m a.g.l over the past 120 hours, and every 6 hours outputted a trajectory, then we integrated all of the calculated data into ten trajectories.

**Figure 10 (A)** Correlation between annual mean precipitation $\delta^{18}O$ ($\delta^{18}O_{ap}$) and local annual mean temperature at Le Mas. **(B)** Correlation between $\delta^{18}O_{ap}$ and local annual mean temperature at Villars. **(C)** Correlation between $\delta^{18}O_{ap}$ and local annual mean

890 precipitation at Le Mas. **(D)** Correlation between $\delta^{18}O_{ap}$ and local annual mean
891 precipitation at Villars.
892 **Figure 11** Back trajectories for initial moisture sources for the 1997-2016 period. The
893 star indicates the location of Villars, and the detailed data of moisture source is listed
894 in Table 2. The air mass history was calculated at 1500 m a.g.l over the past 120 hours,
895 and every 6 hours outputted a trajectory, then we have integrated all of the calculated
896 data into ten trajectories.
897 **Figure 12** Comparison of $\delta^{18}O_{ap}$ and the percentage of initial moisture source (PIMS)
898 and local annual mean temperature and precipitation at Le Mas and Villars on the
899 inter-annual timescale. **(A)** the inter-annual variation of average weighted
900 precipitation $\delta^{18}O$ ($\delta^{18}O_w$), **(B)** the inter-annual average variation of precipitation $\delta^{18}O$
901 ($\delta^{18}O_{ap}$), **(C)** the inter-annual variation of PAWE, **(D)** the inter-annual variation of NA,
902 **(E)** the inter-annual variation of DA, **(F)** the inter-annual variation of NAGR. **(G)** the
903 inter-annual variation of local annual mean temperature in Villars. **(H)** the
904 inter-annual variation of local annual mean precipitation in Villars. The fitting dashed
905 lines indicated the trend for the changes on the inter-annual timescale.
906 **Figure 13** Comparison of the d-excess with the percentage of initial moisture source
907 (PIMS) and the local annual mean temperature at Le Mas and Villars on the
908 inter-annual timescale. **(A)** inter-annual variation of the d-excess at Villars, **(B)**
909 inter-annual variation of the d-excess at Le Mas, **(C)** the inter-annual variation of DA,
910 **(D)** inter-annual variation of NAGR. **(E)** inter-annual variation of local annual mean

911 temperature in Villars. The fitting dashed lines indicates the trend for the changes on

912 the inter-annual timescale.

913

914

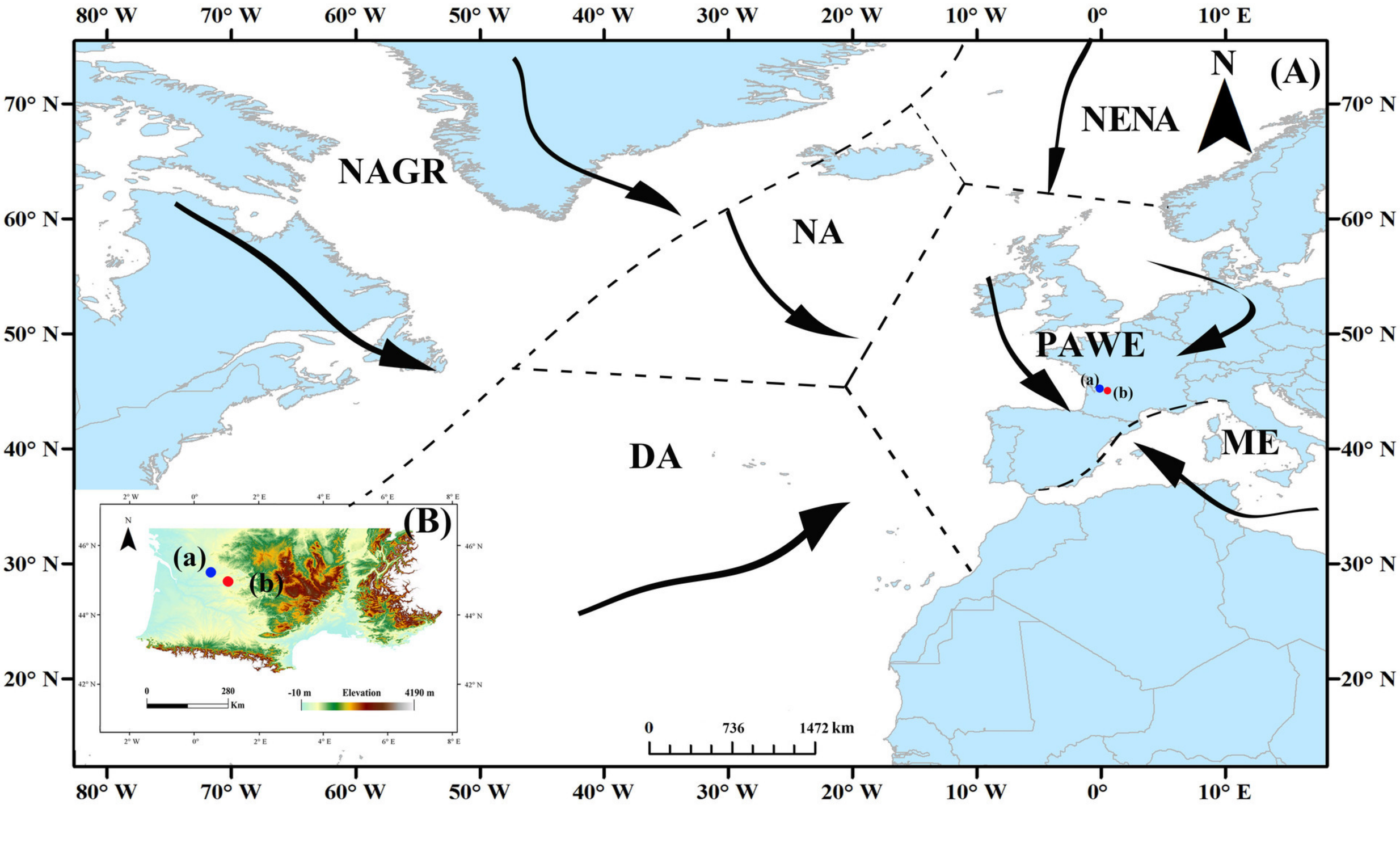
80° W
70° W
60° W
50° W
40° W
30° W
20° W
10° W
0°
10° E
70° N
60° N
50° N
40° N
30° N
20° N
N
(A)
NAGR
NA
NENA
PAWE
ME
DA
(a)
(b)
0
736
1472 km
(B)
2° W
0°
2° E
4° E
6° E
8° E
46° N
44° N
42° N
0
280
Km
-10 m
Elevation
4190 m

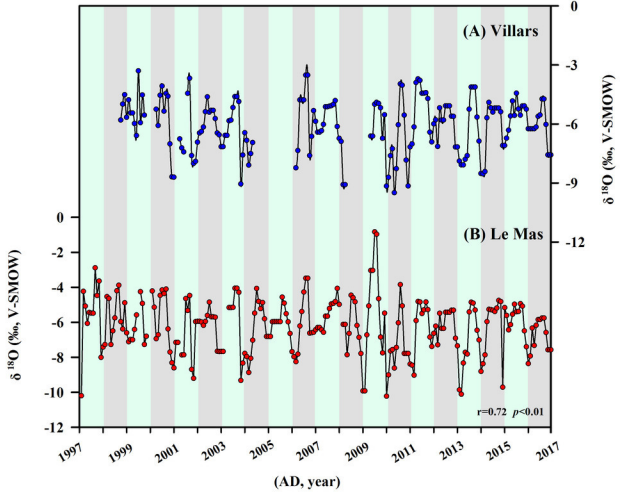
(A) Villars
(B) Le Mas
r=0.72 p<0.01
δ18O (‰, V-SMOW)
δ18O (‰, V-SMOW)
(AD, year)
0
-3
-6
-9
-12
0
-2
-4
-6
-8
-10
-12
1997
1999
2001
2003
2005
2007
2009
2011
2013
2015
2017

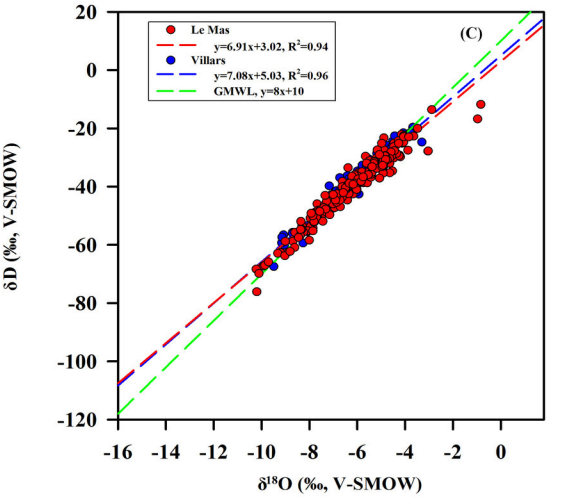
(C)
Le Mas
y=6.91x+3.02, R2=0.94
Villars
y=7.08x+5.03, R2=0.96
GMWL, y=8x+10
δD (‰, V-SMOW)
δ18O (‰, V-SMOW)
20
0
-20
-40
-60
-80
-100
-120
-16
-14
-12
-10
-8
-6
-4
-2
0

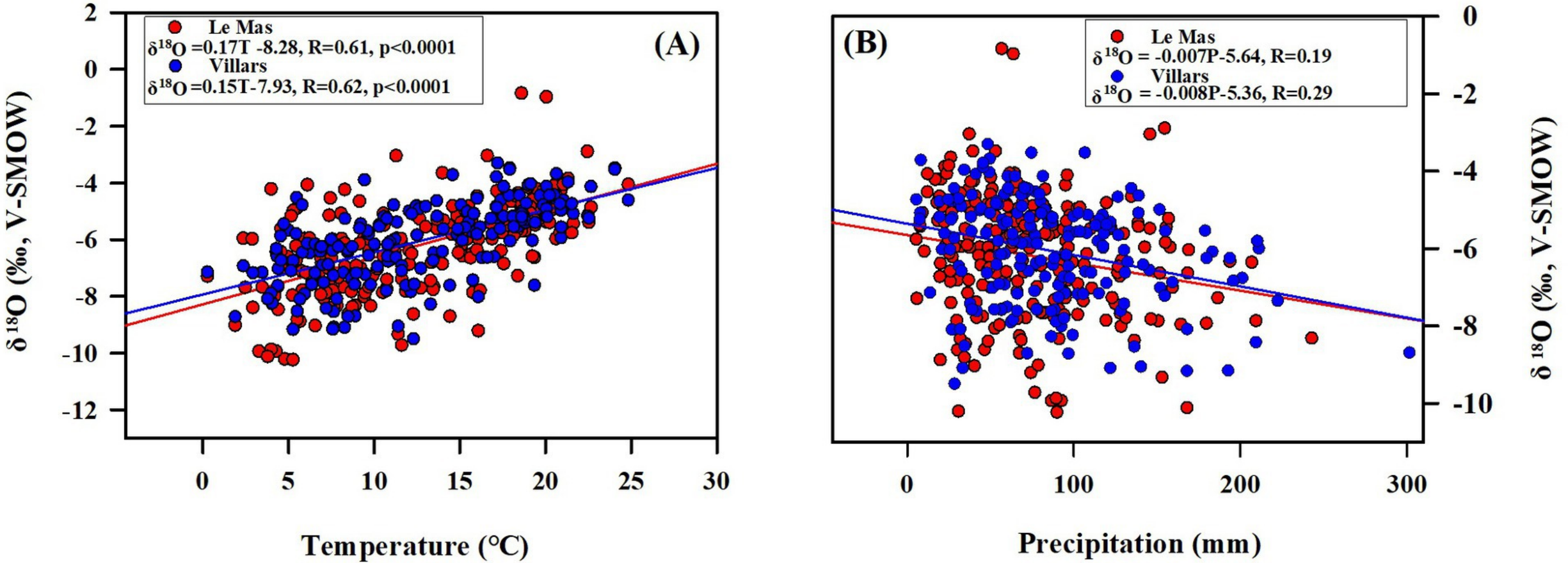
(A)
Le Mas
δ18O =0.17T -8.28, R=0.61, p<0.0001
Villars
δ18O =0.15T-7.93, R=0.62, p<0.0001
δ 18O (‰, V-SMOW)
Temperature (°C)
(B)
Le Mas
δ18O = -0.007P-5.64, R=0.19
Villars
δ18O = -0.008P-5.36, R=0.29
Precipitation (mm)

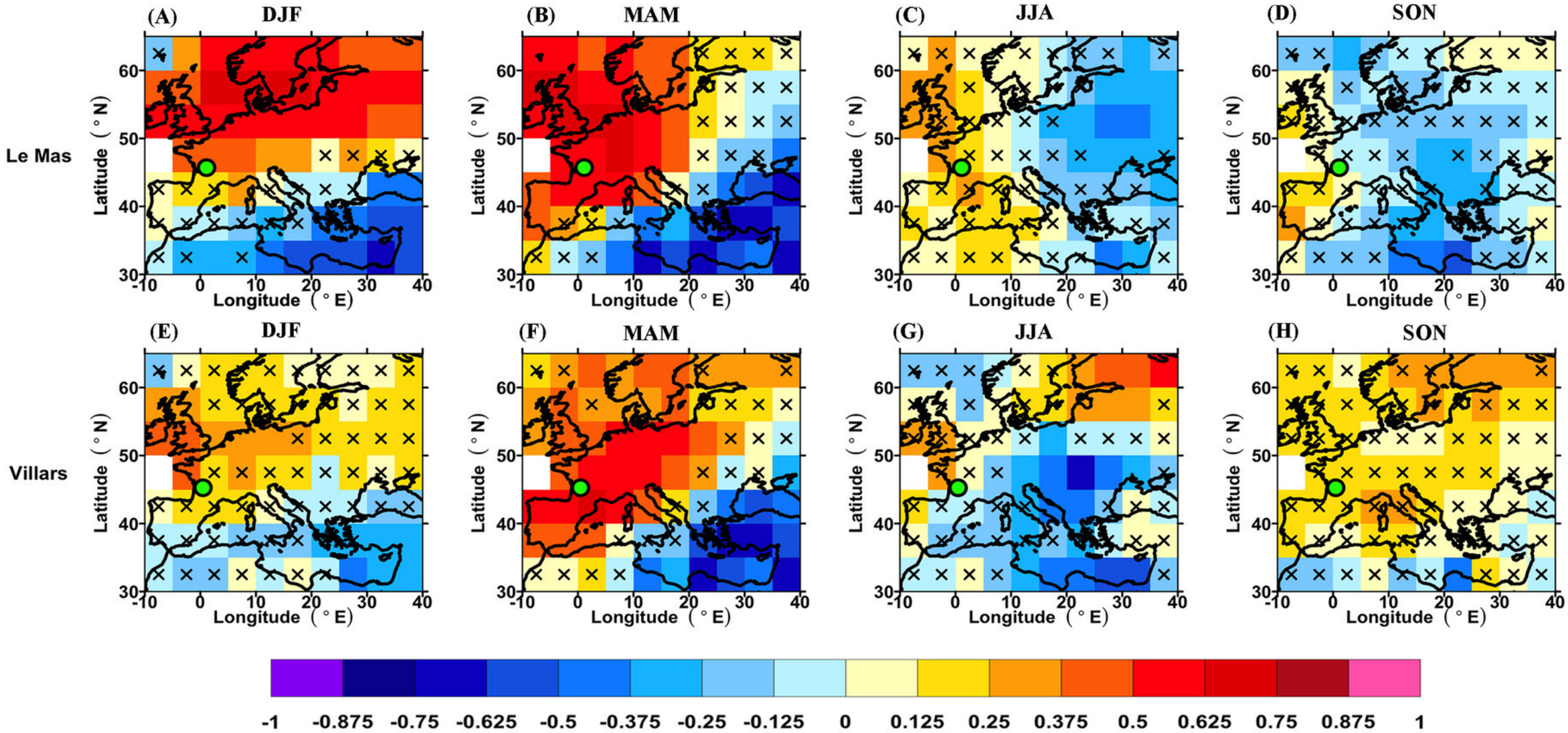
(A) DJF
(B) MAM
(C) JJA
(D) SON
(E) DJF
(F) MAM
(G) JJA
(H) SON
Le Mas
Villars
Latitude ( ° N)
Longitude ( ° E)
-10 0 10 20 30 40
30 40 50 60
-1 -0.875 -0.75 -0.625 -0.5 -0.375 -0.25 -0.125 0 0.125 0.25 0.375 0.5 0.625 0.75 0.875 1

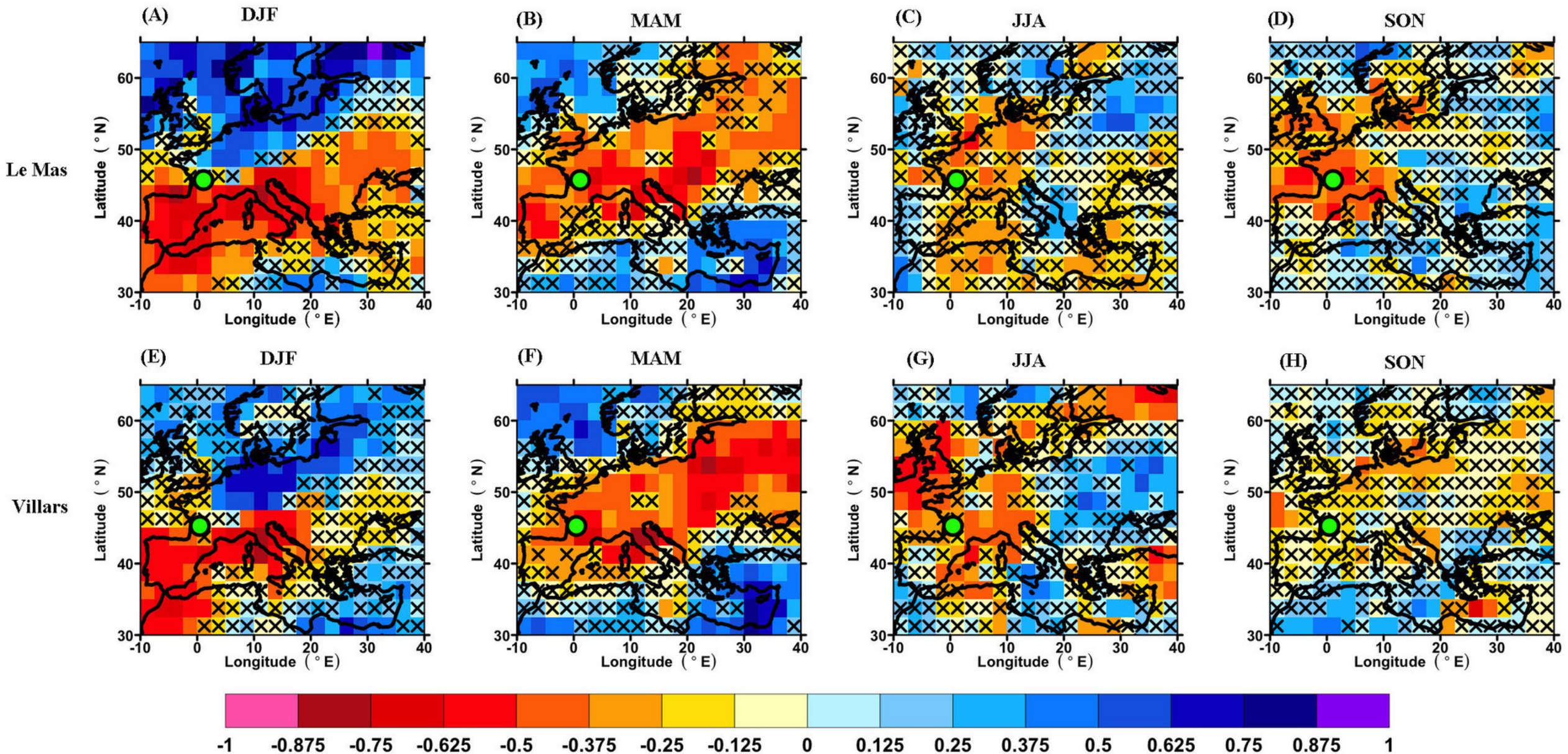
(A) DJF
(B) MAM
(C) JJA
(D) SON
(E) DJF
(F) MAM
(G) JJA
(H) SON
Le Mas
Villars
Latitude ( ° N)
Longitude ( ° E)
-10 0 10 20 30 40
30 40 50 60
-1 -0.875 -0.75 -0.625 -0.5 -0.375 -0.25 -0.125 0 0.125 0.25 0.375 0.5 0.625 0.75 0.875 1

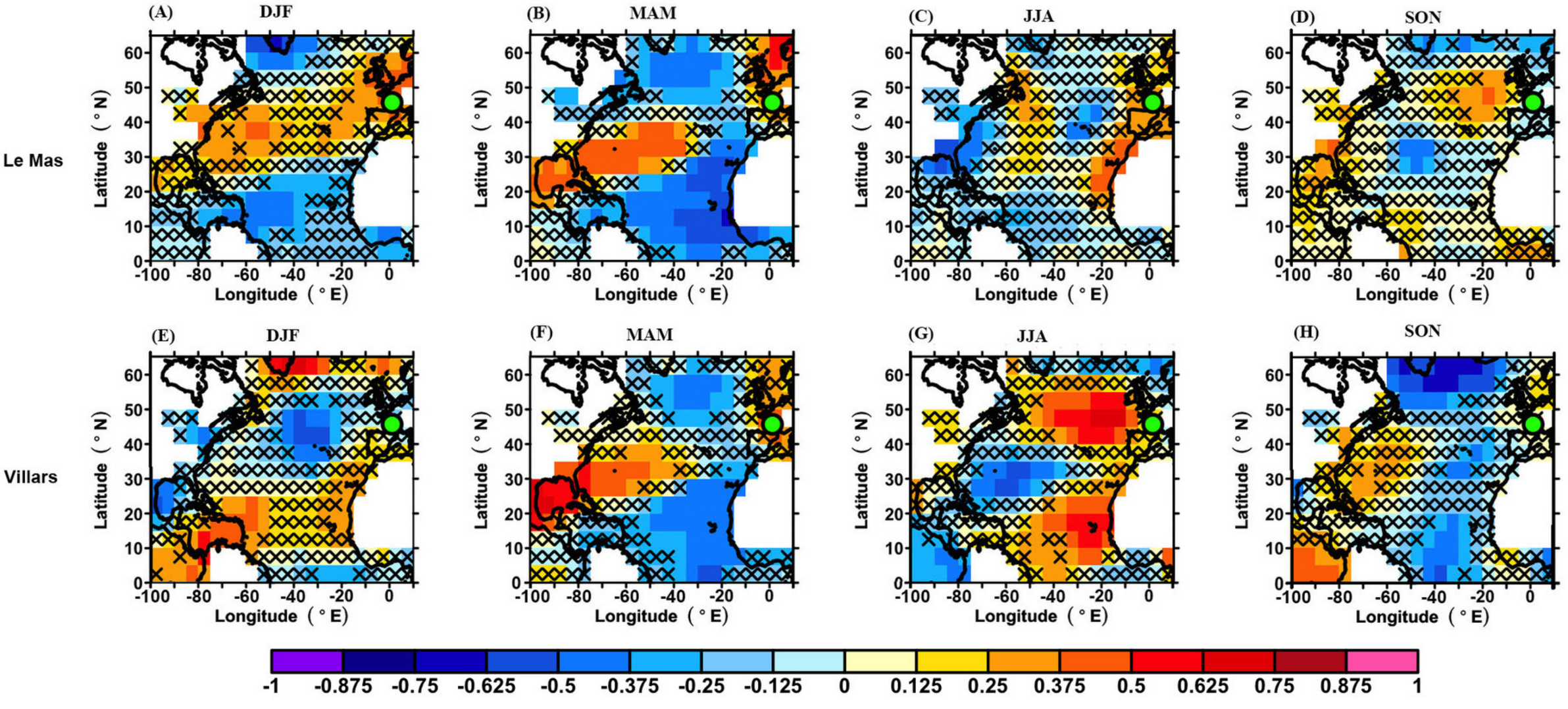
(A) DJF
(B) MAM
(C) JJA
(D) SON
Le Mas
(E) DJF
(F) MAM
(G) JJA
(H) SON
Villars
Latitude ( ° N)
Longitude ( ° E)
-100 -80 -60 -40 -20 0
0 10 20 30 40 50 60
-1 -0.875 -0.75 -0.625 -0.5 -0.375 -0.25 -0.125 0 0.125 0.25 0.375 0.5 0.625 0.75 0.875 1

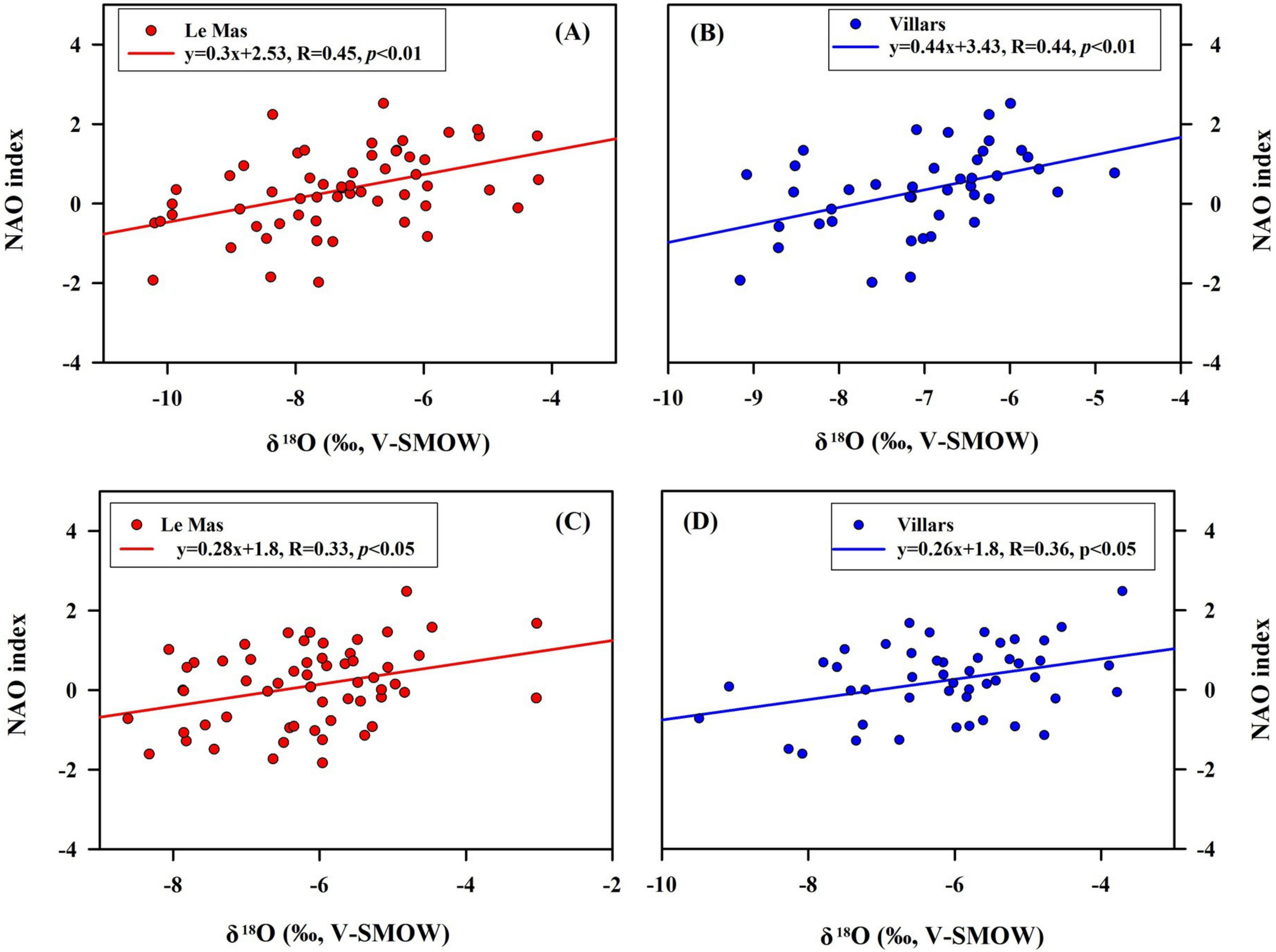
(A)
Le Mas
y=0.3x+2.53, R=0.45, p<0.01
(B)
Villars
y=0.44x+3.43, R=0.44, p<0.01
(C)
Le Mas
y=0.28x+1.8, R=0.33, p<0.05
(D)
Villars
y=0.26x+1.8, R=0.36, p<0.05
NAO index
δ 18O (‰, V-SMOW)

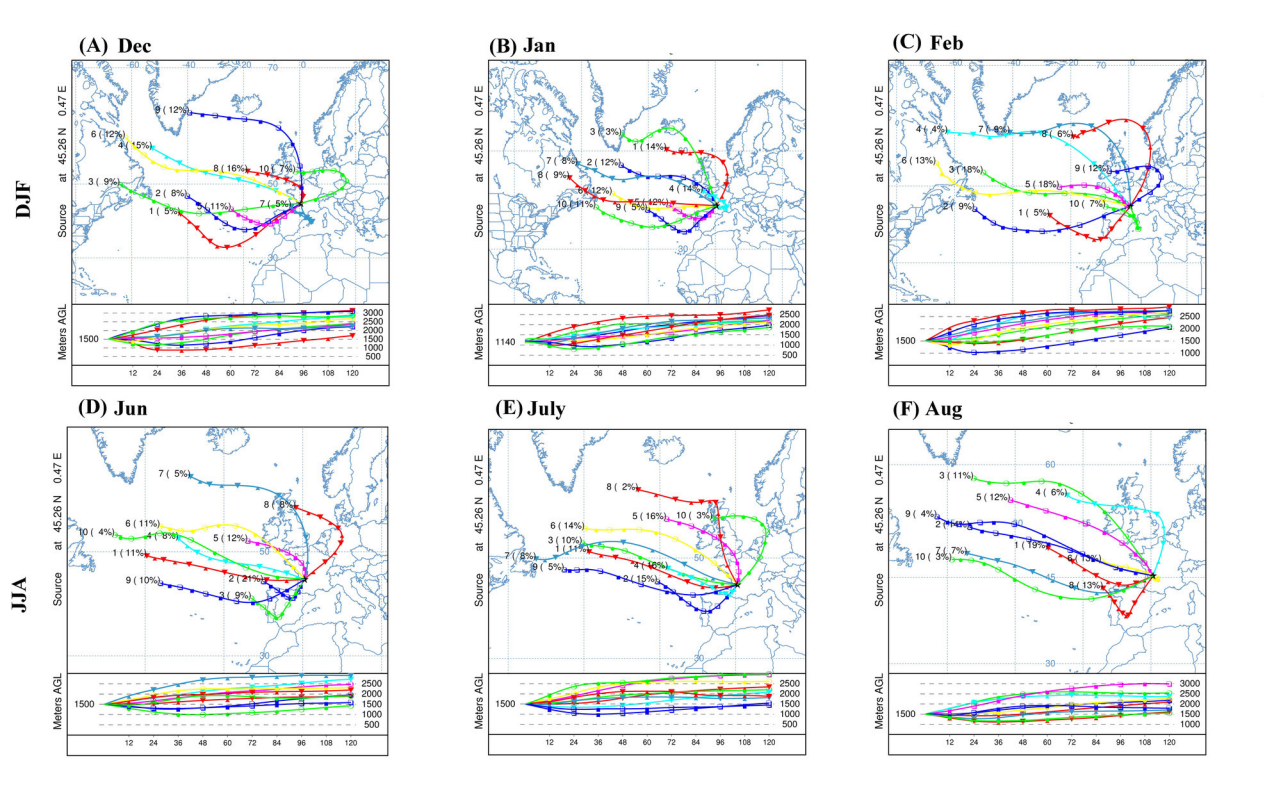
DJF
JJA
(A) Dec
(B) Jan
(C) Feb
(D) Jun
(E) July
(F) Aug
Source at 45.26 N 0.47 E
Meters AGL
1500
1140
12 24 36 48 60 72 84 96 108 120
9 ( 12%)
6 ( 12%)
4 ( 15%)
8 ( 16%)
10 ( 7%)
3 ( 9%)
2 ( 8%)
1 ( 5%)
5 ( 11%)
7 ( 5%)
3 ( 3%)
1 ( 14%)
7 ( 8%)
2 ( 12%)
8 ( 9%)
6 ( 12%)
4 ( 14%)
10 ( 11%)
5 ( 12%)
9 ( 5%)
4 ( 4%)
7 ( 8%)
8 ( 6%)
6 ( 13%)
3 ( 18%)
9 ( 12%)
5 ( 18%)
10 ( 7%)
2 ( 9%)
1 ( 5%)
7 ( 5%)
8 ( 8%)
10 ( 4%)
6 ( 11%)
4 ( 8%)
5 ( 12%)
1 ( 11%)
2 ( 21%)
9 ( 10%)
3 ( 9%)
8 ( 2%)
5 ( 16%)
10 ( 3%)
6 ( 14%)
3 ( 10%)
1 ( 14%)
7 ( 8%)
9 ( 5%)
4 ( 12%)
8 ( 15%)
3 ( 11%)
5 ( 12%)
4 ( 6%)
9 ( 4%)
2 ( 13%)
1 ( 19%)
10 ( 3%)
7 ( 7%)
6 ( 13%)
8 ( 13%)

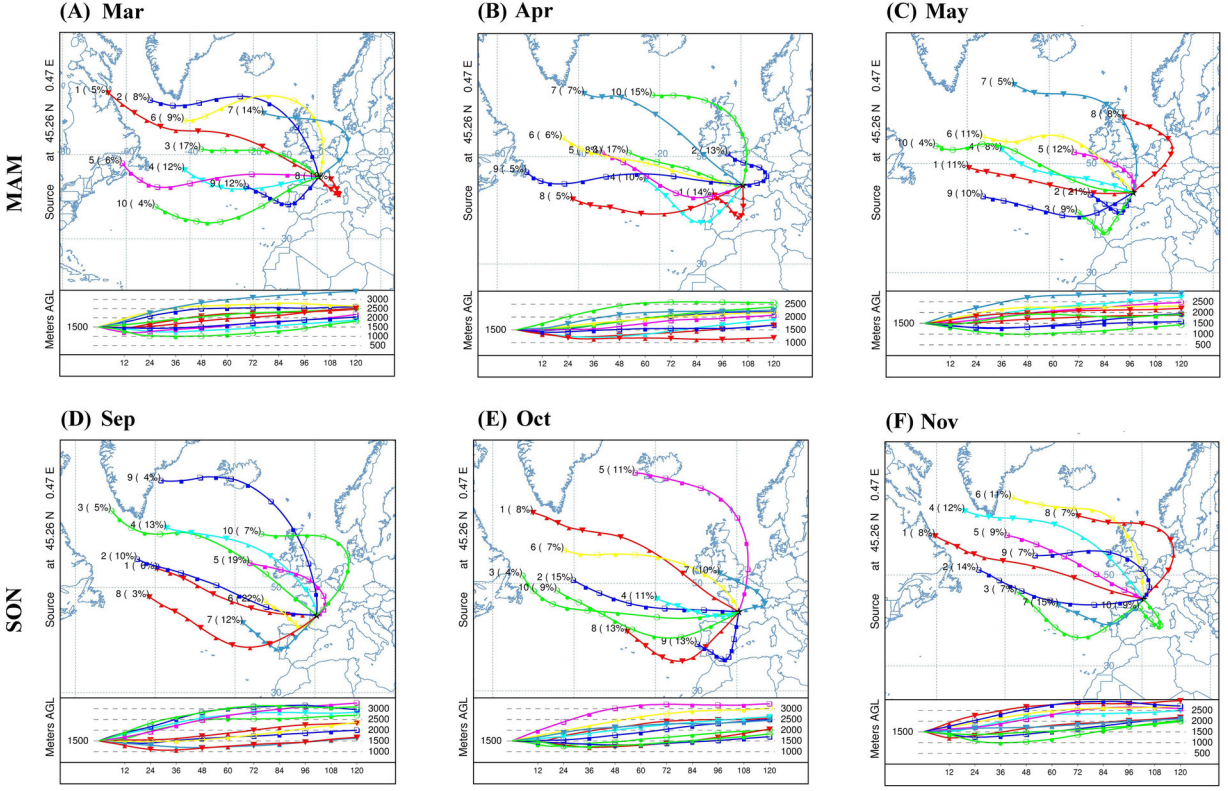
MAM
SON
(A) Mar
(B) Apr
(C) May
(D) Sep
(E) Oct
(F) Nov
Source at 45.26 N 0.47 E
Meters AGL
1500
12 24 36 48 60 72 84 96 108 120
1 ( 5%)
2 ( 8%)
3 ( 17%)
4 ( 12%)
5 ( 6%)
6 ( 9%)
7 ( 14%)
8 ( 12%)
9 ( 12%)
10 ( 4%)
7 ( 7%)
10 ( 15%)
6 ( 6%)
5 ( 8%)
3 ( 17%)
2 ( 13%)
9 ( 5%)
4 ( 10%)
1 ( 14%)
8 ( 5%)
7 ( 5%)
8 ( 8%)
6 ( 11%)
10 ( 4%)
4 ( 8%)
5 ( 12%)
1 ( 11%)
2 ( 21%)
9 ( 10%)
3 ( 9%)
9 ( 4%)
3 ( 5%)
4 ( 13%)
10 ( 7%)
2 ( 10%)
1 ( 6%)
5 ( 19%)
8 ( 3%)
6 ( 22%)
7 ( 12%)
5 ( 11%)
1 ( 8%)
6 ( 7%)
3 ( 4%)
2 ( 15%)
10 ( 9%)
7 ( 10%)
4 ( 11%)
8 ( 13%)
9 ( 13%)
6 ( 14%)
4 ( 12%)
8 ( 7%)
1 ( 8%)
5 ( 9%)
9 ( 7%)
2 ( 14%)
3 ( 7%)
10 ( 15%)

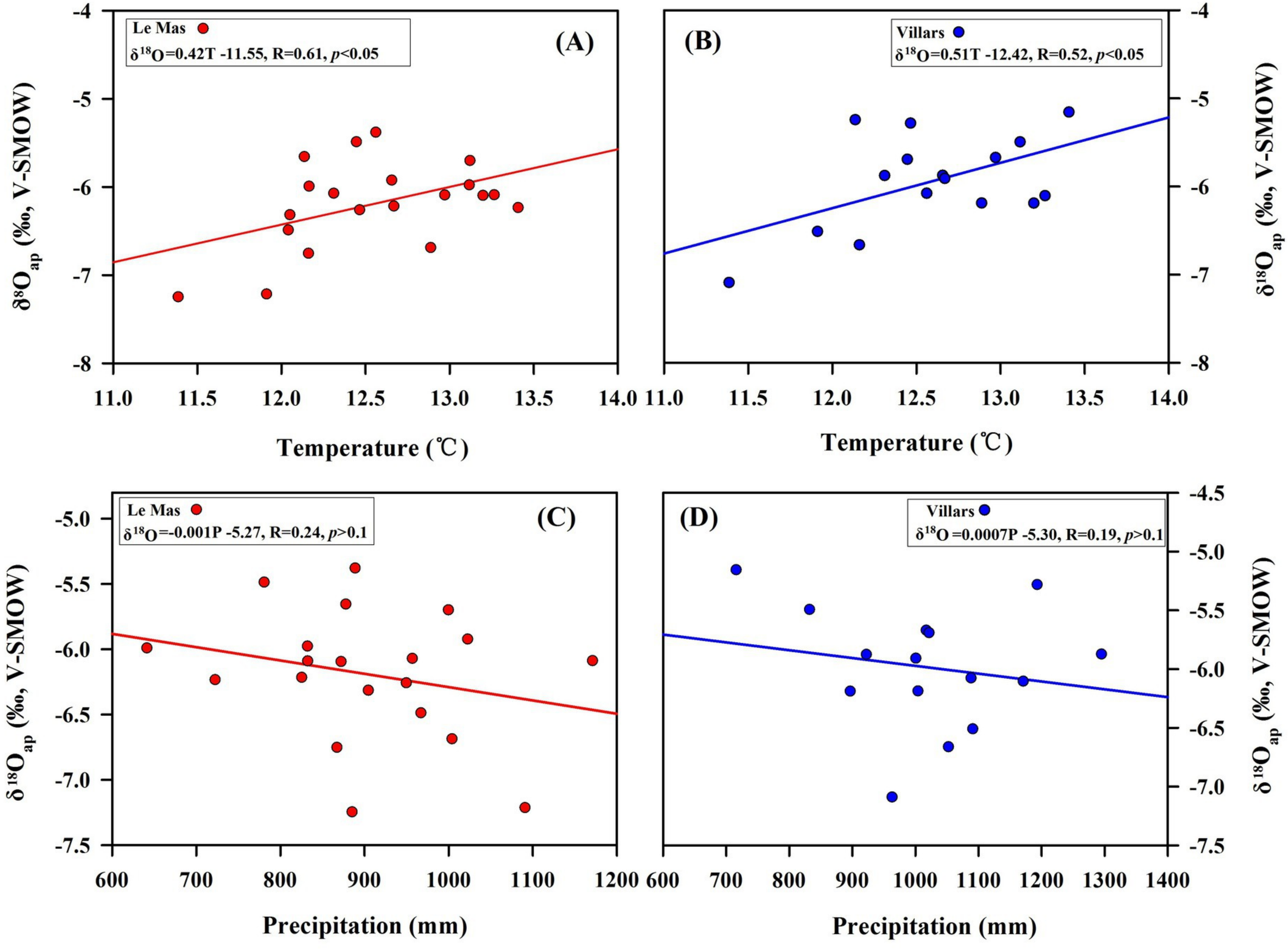
Le Mas
δ18O=0.42T -11.55, R=0.61, p<0.05
(A)
Villars
δ18O=0.51T -12.42, R=0.52, p<0.05
(B)
δ8Oap (‰, V-SMOW)
δ18Oap (‰, V-SMOW)
Temperature (℃)
Le Mas
δ18O=-0.001P -5.27, R=0.24, p>0.1
(C)
Villars
δ18O =0.0007P -5.30, R=0.19, p>0.1
(D)
Precipitation (mm)

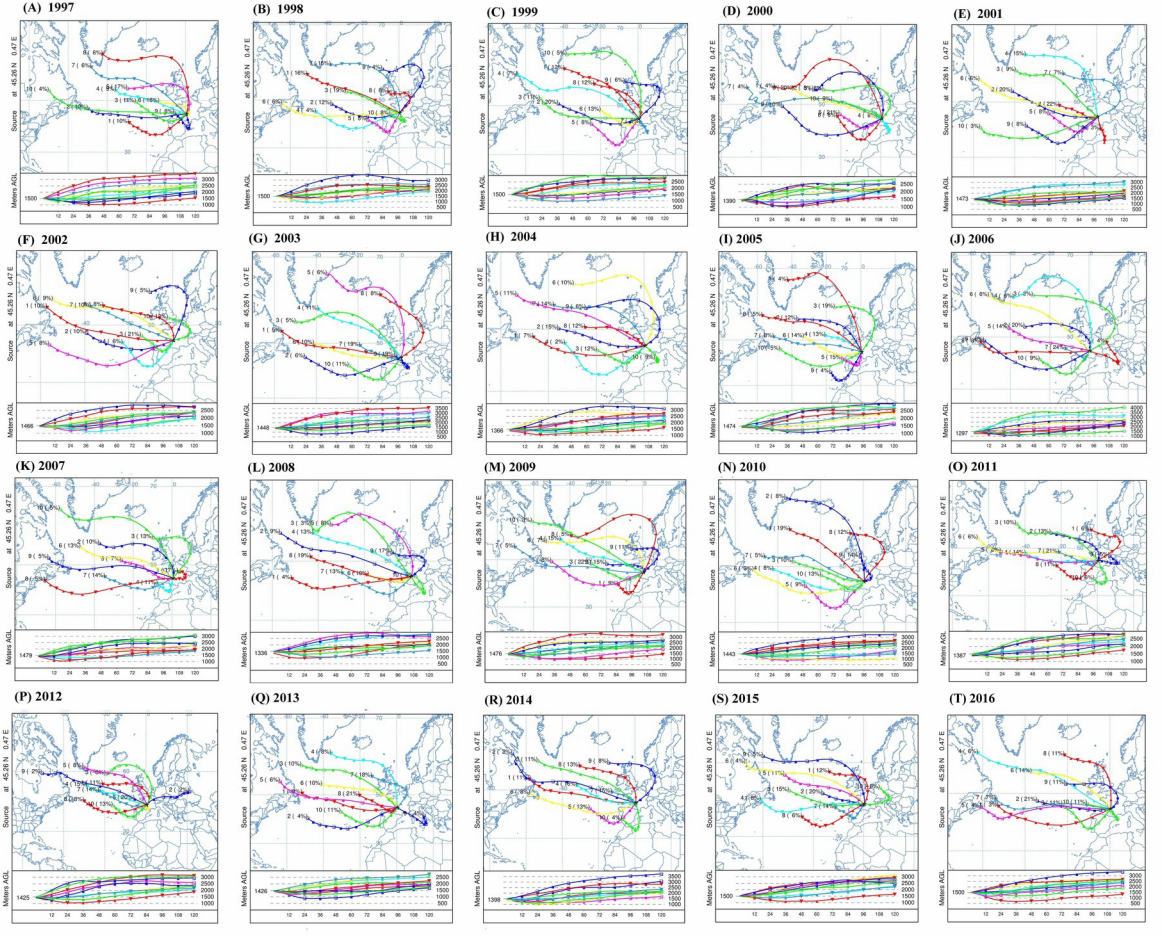
(A) 1997
(B) 1998
(C) 1999
(D) 2000
(E) 2001
(F) 2002
(G) 2003
(H) 2004
(I) 2005
(J) 2006
(K) 2007
(L) 2008
(M) 2009
(N) 2010
(O) 2011
(P) 2012
(Q) 2013
(R) 2014
(S) 2015
(T) 2016
Source
at 45.26 N 0.47 E
Meters AGL

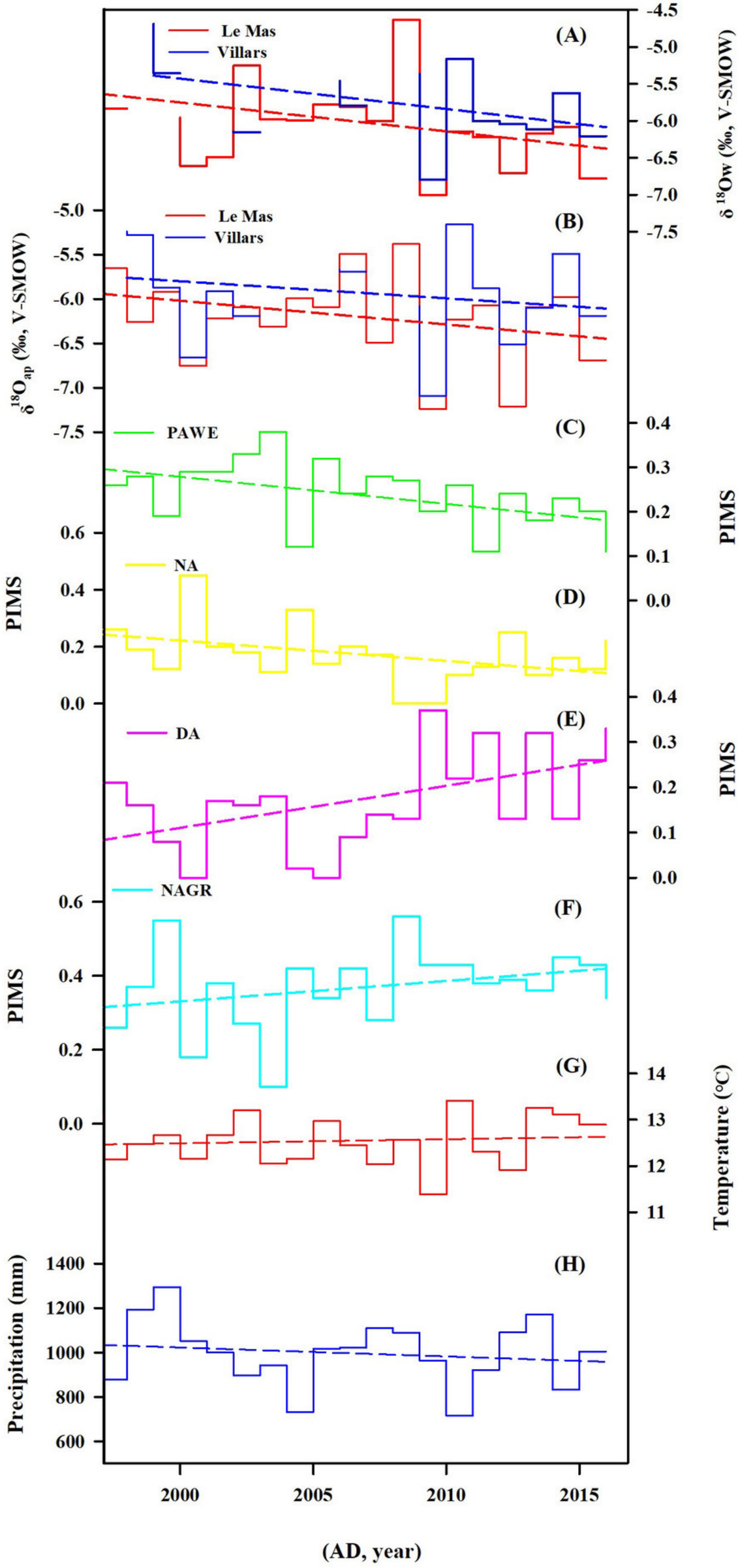
Le Mas
Villars
(A)
-4.5
-5.0
-5.5
-6.0
-6.5
-7.0
-7.5
δ 18Ow (‰, V-SMOW)
(B)
-5.0
-5.5
-6.0
-6.5
-7.0
-7.5
δ18Oap (‰, V-SMOW)
PAWE
(C)
0.4
0.3
0.2
0.1
0.0
PIMS
NA
(D)
0.6
0.4
0.2
0.0
PIMS
DA
(E)
0.4
0.3
0.2
0.1
0.0
PIMS
NAGR
(F)
0.6
0.4
0.2
PIMS
(G)
14
13
12
11
Temperature (°C)
(H)
1400
1200
1000
800
600
Precipitation (mm)
2000
2005
2010
2015
(AD, year)

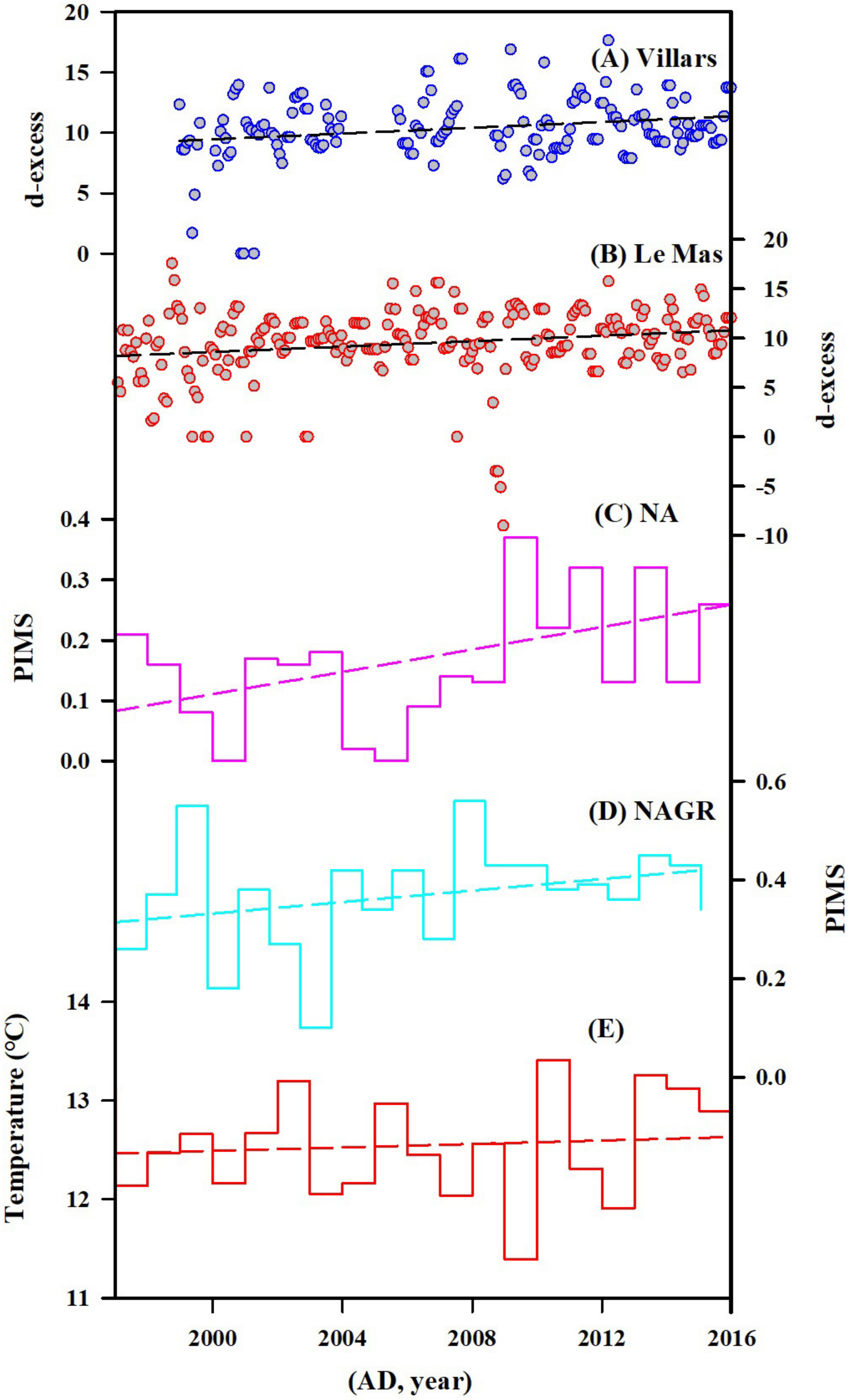
(A) Villars
(B) Le Mas
(C) NA
(D) NAGR
(E)
d-excess
PIMS
Temperature (°C)
20
15
10
5
0
-5
-10
0.4
0.3
0.2
0.1
0.0
0.6
14
13
12
11
2000
2004
2008
2012
2016
(AD, year)

## Tables

Table1 Size by size proximate analysis (as received basis).

| Particle size (µm) | Values in (%) | | | | |
|---|---|---|---|---|---|
| | Weight | Ash | Moisture | Volatile matter | Fixed carbon |
| -500+340 | 14.2 | 35.4 | 2.1 | 21.1 | 41.5 |
| -340+250 | 20.1 | 33.4 | 2.0 | 21.4 | 43.3 |
| -250+180 | 6.5 | 30.9 | 2.2 | 20.9 | 46.1 |
| -180+125 | 16.2 | 29.3 | 2.5 | 20.5 | 47.8 |
| -125+90 | 7.9 | 30.6 | 2.4 | 21.1 | 45.9 |
| -90+75 | 10.0 | 36.1 | 2.3 | 20.2 | 41.4 |
| -75+42 | 19.6 | 46.7 | 2.1 | 20.6 | 30.7 |
| -42 | 5.5 | 50.8 | 3.2 | 15.9 | 30.2 |
| Calculated Head | - | 34.7 | 2.7 | 20.4 | 42.3 |

Table 2 Operating conditions of flotation machine

| Operating parameter | Values |
|---|---|
| Solid concentration during conditioning with reagents, % (w/w) | 40 |
| Collector dosage, kg/ton | 0.5 |
| Frother dosage, kg/ton | 0.25 |
| Agitation time, seconds | 300 |
| Conditioning time with collector, seconds | 120 |
| Conditioning time with frother, seconds | 60 |
| Initial solid concentration for flotation, %(w/w) | 10 |
| Froth collection time, seconds | 5, 10, 15, 30, 60, 90, 120 |
| pH of the slurry | 7.2 |

Table 3 Performance of three cells for different impeller speeds at different target ash

| Impeller Speed: 1200 rpm | | | | | | | | | |
|---|---|---|---|---|---|---|---|---|---|
| Target Ash% | 2 L | | | 4 L | | | 6 L | | |
| | Yield (%) | Time (s) | Com. Recovery (%) | Yield( %) | Time (s) | Com. Recovery( %) | Yield (%) | Time (s) | Com. Recovery( %) |
| 12 | - | - | - | - | - | - | 9 | 5 | 12 |
| 13 | - | - | - | 20 | 7 | 29 | 30 | 29 | 41 |
| 14 | - | - | - | 32 | 22 | 45 | 40 | 120 | 53 |
| 15 | - | - | - | (50) | 120 | 67 | - | - | - |
| 16 | 30 | 12 | 39 | - | - | - | - | - | - |
| 17 | 39 | 40 | 50 | - | - | - | - | - | - |
| 18 | (45) | 120 | 57 | - | - | - | - | - | - |
| Impeller Speed: 1500 rpm | | | | | | | | | |
| Target Ash% | 2 L | | | 4 L | | | 6 L | | |
| | Yield % | Time (s) | Com. Recovery % | Yield % | Time (s) | Com. Recovery % | Yield % | Time (s) | Com. Recovery % |
| 14 | - | - | - | - | - | - | 39 | 29 | 53 |
| 15 | - | - | - | 29 | 6 | 37 | (47) | 120 | 62 |
| 16 | - | - | - | 40 | 12 | 51 | - | - | - |
| 17 | | - | - | (54) | 60 | 68 | - | - | - |
| 18 | 27 | 25 | 35 | - | - | - | - | - | - |
| 19 | 35 | 90 | 44 | - | - | - | - | - | - |
| Impeller Speed: 1800 rpm | | | | | | | | | |
| Target | 2 L | | | 4 L | | | 6 L | | |

| Ash% | Yield % | Time (s) | Com. Recovery % | Yield % | Time (s) | Com. Recovery % | Yield % | Time (s) | Com. Recovery % |
|---|---|---|---|---|---|---|---|---|---|
| 17 | - | - | - | - | - | - | 54 | 110 | 70 |
| 18 | - | - | - | 48 | 50 | 63 | - | - | - |
| 22 | 21 | 12 | 26 | - | - | - | - | - | - |
| 23 | 31 | 100 | 35 | - | - | - | - | - | - |

Table 4. Ultimate combustible recovery with corresponding rate constants in different cells at different impeller speeds

| Parameters | Impeller speed (rpm) | | | | | | | | |
|---|---|---|---|---|---|---|---|---|---|
| | 1200 | | | 1500 | | | 1800 | | |
| | 2 L | 4 L | 6 L | 2 L | 4 L | 6 L | 2 L | 4 L | 6 L |
| $R_\infty$ (%) | 57.1±0.25 | 71.7±0.71 | 61.7±7.61 | 48.8±1.73 | 72.4±0.71 | 61.5±0.51 | 38.2±1.77 | 68.4±0.25 | 70.8±0.93 |
| $\phi$ (%) | 30.1±1.19 | 35.5±0.75 | 14.8±5.01 | 14.4±1.56 | 30.6±3.18 | 32.1±2.27 | 11.9±2.86 | 30.3±1.42 | 34.9±8.14 |
| $K_f$ ($s^{-1}$) | 0.533±0.015 | 0.147±0.004 | 0.062±0.007 | 0.136±0.011 | 0.284±0.037 | 0.311±0.039 | 0.205±0.039 | 0.294±0.015 | 0.249±0.061 |
| $K_s$ ($s^{-1}$) | 0.039±0.002 | 0.017±0.001 | 0.004±0.003 | 0.016±0.006 | 0.036±0.005 | 0.043±0.004 | 0.023±0.014 | 0.046±0.002 | 0.051±0.012 |
| SSE | 2.31 | 0.06 | 0.32 | 0.28 | 0.10 | 0.46 | 1.31 | 0.13 | 1.80 |
| $R^2$ | 1.00 | 1.00 | 1.00 | 1.00 | 1.00 | 1.00 | 0.99 | 1.00 | 1.00 |
| Adjusted $R^2$ | 0.99 | 1.00 | 1.00 | 1.00 | 1.00 | 1.00 | 0.99 | 1.00 | 1.00 |
| RMSE | 1.07 | 0.17 | 0.40 | 0.38 | 0.22 | 0.48 | 0.81 | 0.25 | 0.95 |

Table 5 ANOVA derived for yield, ash content, combustible recovery and entrained water recovery models

| Statistics | Yield | Ash | Combustible recovery | Entrained water recovery |
|---|---|---|---|---|
| Sum of squares | 594.13 | 58.07 | 1118.30 | 694.01 |
| Degree of freedom | 5 | 2 | 5 | 2 |
| Mean square | 118.83 | 29.03 | 223.66 | 347 |
| F-value | 22.81 | 47.62 | 62.82 | 106.6 |
| p-value | 0.0136 | 0.0002 | 0.0031 | <0.0001 |
| Standard deviation | 2.28 | 0.78 | 1.89 | 1.8 |
| $R^2$ | 0.97 | 0.94 | 0.99 | 0.97 |
| Adjusted $R^2$ | 0.93 | 0.92 | 0.97 | 0.96 |
| Equation | Quadratic | Linear | Quadratic | Linear |

Table 6 ANOVA results showing the terms in each response for their respective models

| Response | Source | Sum of Squares | Mean Square | F-value | p-value | Remark |
|---|---|---|---|---|---|---|
| Yield | A | 2.67 | 0.53 | 0.51 | 0.526 | NS |
| | B | 115.19 | 23.04 | 22.11 | 0.0182 | S |
| | AB | 217.27 | 43.45 | 41.71 | 0.0075 | S |
| | $A^2$ | 2.04 | 0.41 | 0.39 | 0.5758 | NS |
| | $B^2$ | 256.96 | 51.39 | 49.33 | 0.0059 | S |
| Ash | A | 23.36 | 11.68 | 38.32 | 0.0008 | S |
| | B | 34.70 | 17.35 | 56.92 | 0.0003 | S |
| Combustible recovery | A | 0.03 | 0.01 | 0.01 | 0.9302 | NS |
| | B | 324.14 | 64.83 | 91.04 | 0.0024 | S |
| | AB | 354.38 | 70.88 | 99.53 | 0.0021 | S |
| | $A^2$ | 2.66 | 0.53 | 0.75 | 0.4509 | NS |
| | $B^2$ | 437.09 | 87.42 | 122.77 | 0.0016 | S |
| Entrained water recovery | A | 369.58 | 184.79 | 113.54 | < 0.0001 | S |
| | B | 324.43 | 162.22 | 99.67 | < 0.0001 | S |
| *Notes: A: Impeller speed; B: Cell volume; S: Significant; NS: Not significant* | | | | | | |